Airplane Design Optimization for Minimal Global Warming Impact

Pieter-Jan Proesmans* and Roelof Vos[†]
Delft University of Technology, Kluyverweg 1 2629HS, Delft, The Netherlands

This paper presents a method to assess the key performance indicators of aircraft designed for minimum direct operating cost and aircraft designed for minimum global warming impact. The method comprises a multidisciplinary aircraft optimization algorithm capable of changing wing, engine and mission design variables while including constraints on flight and field performance. The presented methodology uses traditional Class-I methods augmented with dedicated Class-II models to increase the sensitivity of the performance indicators to relevant design variables. The global warming impact is measured through the average temperature response caused by several emission species, including CO_2, NO_x and contrail formation, over a prolonged period of one hundred years. The analysis routines are verified against experimental data or higher-order methods. The design algorithm is subsequently applied to a single-aisle, medium-range aircraft, demonstrating that a 57% reduction in average temperature response can be achieved compared to an aircraft optimized for minimal operating costs. This reduction is realized by flying at 7.6 km and Mach 0.60, and by lowering the engine overall pressure ratio to approximately 37. However, to compensate for the lower productivity, it is estimated that 13% more climate-optimized aircraft have to be operated for the hypothetical fleet under consideration.

Nomenclature

A	=	aspect ratio [-] or cross-sectional area [m^2]
b	=	wing span [m]
c	=	chord length [m] or climb rate [m/s]
$\bar{c}$	=	length of mean aerodynamic chord[m]
C_L	=	aircraft lift coefficient [-]

*PhD Candidate, Faculty of Aerospace Engineering, P.Proesmans@tudelft.nl, AIAA Student Member, Corresponding Author
[†]Assistant Professor, Faculty of Aerospace Engineering, R.Vos@tudelft.nl, AIAA Associate Fellow

C_D	=	aircraft drag coefficient [-]
C_{D_0}	=	zero-lift drag coefficient [-]
C_{ops}	=	operating costs [USD/(seat · nm) or USD]
d	=	diameter [m]
E_i	=	emission of species i [kg]
EI_i	=	emission index of species i [kg/kg]
e	=	Oswald factor [-]
h	=	altitude [m or ft]
l	=	length [m]
m	=	mass [kg]
$\dot{m}$	=	mass flow [kg/s]
M	=	Mach number [-]
N	=	integer number or amount [-]
p	=	pressure [N/m^2]
r_{bl}	=	block range [km]
S	=	surface area [m^2]
T	=	thrust [kN] or temperature [K]
t_{bl}	=	block time [hours]
t/c	=	Chord thickness [-]
U_{ann}	=	annual utilization [hours/year]
V	=	velocity [m/s]
$\bar{V}$	=	volume coefficient [-]
W	=	weight [kN]
x	=	absolute, longitudinal coordinate [m]
$\mathbf{x}$	=	design vector
γ	=	ratio of specific heats [-]
ΔT	=	surface temperature change [K]
$\Lambda_{0.25}$	=	wing quarter-chord sweep angle [deg]
λ	=	wing taper ratio [-]
ξ	=	longitudinal coordinate relative to MAC [-]
ρ	=	density [kg/m^3]
χ_i	=	concentration of species i [ppmv]

Subscripts

0	=	sea-level condition or initial value
0.25	=	measured at quarter-chord
AC	=	evaluated for one aircraft
ann	=	annually
app	=	approach condition
core	=	core flow
cr	=	cruise condition
eng	=	engine
fe	=	fixed equipment
FG	=	fuselage group
fleet	=	evaluated for the entire fleet
fuel	=	fuel
fus	=	fuselage
ht	=	horizontal tail
nac	=	nacelle
root	=	chord
tip	=	tip chord
TO	=	take-off condition
vt	=	vertical tail
w	=	wing
WG	=	wing group
∗	=	optimal solution

I. Introduction

THE fact that aviation contributes to global warming is well-established [1, 2]. It is estimated that in 2011, aviation resulted in approximately 3.5% of the net anthropogenic effective radiative forcing (ERF), of which 66% is caused by non-CO_2 contributions, acknowledging the remaining uncertainties [2]. Although this net effect may seem relatively small, it is important to note that the aviation transport industry grows fast compared to other transport sectors, by approximately 4 to 5% annually in terms of revenue passenger kilometer (RPK) [3, 4], ignoring the potential influence of the Corona virus pandemic in 2020. Hence, technological advancements, operational changes, new policies or any combination thereof might have to be adopted to reduce aviation's impact. However, radical solutions implemented in

land-based transportation, such electric propulsion, cannot as easily be adopted in commercial aircraft.

Previous studies have revealed that the objective of minimizing the global warming impact, from an aircraft design perspective, does not align with the objective of minimizing direct operating costs (DOC) [5–7]. Even when the minimization of fuel consumption is considered as the overall design objective, this still does not result in an airframe and engine combination which has a minimal impact on global warming due to non-CO_2 effects [8].

In Ref. [5], Antoine and Kroo carry out a multi-objective optimization of both aircraft and engine design variables for four individual design objectives: minimal DOC, minimal fuel burn, minimal NO_x emissions and minimal noise. In their research, the climate impact of an aircraft is assessed by the emissions (in kg or lb) of CO_2 over the entire flight as well as the NO_x emissions in the landing and take-off (LTO) cycle. These two cost functions are considered individually since it is assumed that NO_x emissions in cruise are insignificant with respect to the emissions of CO_2 (and CO and SO_2) in cruise. A similar approach is taken by Henderson et al. [9] and Chai et al. [10]. Although the NO_x emissions in LTO are of interest and ICAO regulations are imposed, this measure does not account for the effect of NO_x at high altitudes due its influence on short-term ozone (O_3) creation and long-term methane (CH_4) and ozone depletion. Such indirect effects on global warming, and other effects such as contrails and contrail cirrus, have to be determined through more advanced climate models and more comprehensive metrics. Examples of the latter are the average temperature response (ATR) [6, 7, 11] and the global warming potential (GWP) [12].

Later studies by Dallara and Kroo [7] and Koch [13] included more advanced models and metrics in aircraft optimization routines. The former adopted a linearized climate model with altitude variations, providing an average climate response with limited computational power, while the latter employed the more detailed AirClim model by Grewe and Stenke [14]. Although the numerical results of these studies cannot be compared directly, the trends in aircraft design parameters appear to be similar. For example, when changing the design objective from the minimization of DOC to the minimization of the average temperature response, it can be observed that the wing aspect ratio increases, the wing gets less sweep back, the cruise Mach number reduces and the cruise altitude is lowered. While only operational changes, such as a different cruise altitude and Mach number, can already reduce the climate impact of the original aircraft, the financial cost rise can be limited by an optimized redesign.

The studies by Koch, Dallara and Kroo can be further extended by including more turbofan design variables such as overall pressure ratio (OPR) and turbine entry temperature (TET). Research conducted in NASA's Environmentally Responsible Aviation (ERA) project, among others, has explored the influence of a higher OPR and increased bypass ratio (BPR) on the fuel burn, LTO NO_x and noise [15]. Although it was shown that such engine cycle modifications can yield a significant reduction in fuel burn (33 to 45% for a large, single-aisle aircraft), they may have an adverse effect on non-CO_2 climate effects. Raising the OPR and TET, for example, increases the formation of thermal NO_x [16], although the emission index of NO_x in LTO and cruise can be further reduced through future combustor technologies [17]. Additionally, increasing the bypass ratio of turbofan engines increases the probability of contrail formation [18]. This

demonstrates that optimizing for minimum fuel burn, again, does not necessarily align with the objective of minimizing global warming impact.

Although flying slower may be one effective measure to reduce the climate impact of an aircraft design, it increases the mission block time. For a constant travel demand, this productivity loss has to be covered by carrying more passengers per flight or by increasing the number of aircraft in the fleet. Several research projects have highlighted the importance of a complete fleet-level analysis in the assessment of new technologies and have proposed advanced modeling frameworks [19–21] in which the aircraft flight profiles have to be simulated [22]. Research by Moolchandani et al. and Jimenez et al. employed fleet-level models to assess the environmental impact of future technologies considered in the ERA project [23, 24]. It was concluded that introduction of ERA technologies can lower the fleet-total fuel burn sufficiently to sustain carbon-neutral operational growth in the future, according to the goals set worldwide, although a discussion of non-CO_2 climate effects is not included.

Building upon these observations from previous research, it is of interest to study what combination of turbofan, airframe, and operational design variables minimize a comprehensive climate metric while monitoring the potential impact on the fleet operations. The research presented in this paper, therefore, aims at answering the following question: How do the airplane design variables, defined by wing, engine and mission design variables, change when shifting from a direct-operating-cost objective towards a climate-impact objective?

To answer this question, a design methodology is proposed capable of capturing interrelated effects of all relevant disciplines. Furthermore, the temporal effects of CO_2, NO_x and induced cloudiness have to be assessed employing one comprehensive metric. The current scope is limited to a classic tube-and-wing configuration, with kerosene-fueled turbofan engines mounted to the wing and using state-of-the art technology. Other environmental aspects, such as noise and air quality are not taken into account in the current study.

While it is recognized that operational changes and trajectory optimizations can further reduce the fuel burn [25, 26] and ATR [27], such improved operational schemes are outside the scope of the current study. Nevertheless, it is recommended to perform a simultaneous optimization of the aircraft design and operations to minimize the climate impact, including non-CO_2 effects, in the future employing similar approaches as taken in previous studies [23, 28].

The paper is structured as follows. Following this introduction, Section II defines the optimization problem and elaborates the multidisciplinary design methodology. All the relevant analysis methods are explained in this section. Subsequently, validation of the analysis methods is performed in Section III along with the verification of the design methodology. Section IV presents the results of the optimization study tailored towards a medium-range, single-aisle aircraft and answers the research question introduced above. Finally, the most important conclusions are gathered in Section V along with recommendations for further studies.

II. Problem Formulation and Methodology Description

To answer the research question proposed in the introduction, a multidisciplinary design and optimization routine is developed. This chapter discusses the arrangement of the implemented framework tailored to the current research aim. Section II.A focuses on the definition of the optimization problem and the overall strategy, followed by Section II.B which discusses the methods of the individual analyses and design disciplines.

A. Design and Optimization Problem

One can optimize an aircraft design to achieve minimal average temperature response (ATR), minimal cash operating costs (COC or C_{ops}) or minimal mission fuel burn (m_{fuel}). However, previous research has indicated that these objectives result in different airplane designs with different performance indicators. To study the difference between the three, a single-objective optimization problem is defined as follows:

$$
\begin{aligned}
\underset{\mathbf{x}}{\text{minimize}} \quad & F\left(\mathbf{x}\right) = \mathrm{ATR}_{100}\left(\mathbf{x}\right) \quad \text{or} \quad C_{\mathrm{ops,fleet}}\left(\mathbf{x}\right) \quad \text{or} \quad m_{\mathrm{fuel,fleet}}\left(\mathbf{x}\right) \\
\text{subject to} \quad & W/S \leq \frac{1}{2}\rho_0 \left(\frac{V_{\mathrm{app}}}{1.23}\right)^2 C_{L_{\mathrm{max}}}, \\
& b \leq b_{\mathrm{max}}, \\
& \mathrm{TET}_{\mathrm{TO}} \leq \mathrm{TET}_{\mathrm{TO,\,max}}, \\
& C_{L_{\mathrm{cr}}} \leq \frac{C_{L_{\mathrm{buffet}}}}{1.3} = \frac{0.86 \cdot \cos \Lambda_{0.25}}{1.3}, \\
& C_{L_{\mathrm{max}}} \leq 2.8 \cdot \cos \Lambda_{0.25}, \\
& x_i^L \leq x_i \leq x_i^U \qquad\qquad \text{for } i = 1, 2, ..., 10
\end{aligned}
\tag{1}
$$

Since the climate impact is assessed for a complete fleet, the costs and fuel usage are evaluated in a similar manner, denoted by the fleet subscript. The design vector $\mathbf{x}$ contains the variables related to the airframe, engine and mission. A summary of these variables and their lower ($\mathbf{x}^L$) and upper ($\mathbf{x}^U$) bounds is provided in Table 1. For the airframe, the aspect ratio (A), wing loading (W/S) and maximum lift coefficient ($C_{L_{\mathrm{max}}}$) are used as the prime design variables, where the maximum lift coefficient is related to the design of the high-lift devices. The engine design is governed by the bypass ratio, the pressure ratios of the individual compressor elements (Π_i), as well as the turbine entry temperature (TET). The mission design variables comprise the cruise Mach number (M_{cr}) and the cruise altitude (h_{cr}).

The optimization definition in Equation (1) includes five constraints. The first one imposes a limit on the wing loading due to the required minimum approach speed V_{app} at the selected $C_{L_{\mathrm{max}}}$. The single-aisle, medium range jet aircraft of interest is considered to belong to ICAO aircraft approach category C, resulting in an approach speed of approximately 135 to 140 kts (69 to 72 m/s). A constraint is introduced for the maximum turbine entry temperature at take-off. $\mathrm{TET}_{\mathrm{TO,\,max}}$ is assumed to be 2000 K according to the insights by Mattingly et al.. The third constraint dictates

Table 1   Design variables and their respective bounds and initial values

Variable	Description [Unit]	Lower Bound (x^L)	Upper Bound (x^U)
W/S	Wing loading [kN/m^2]	3.00	7.00
A	Aspect ratio [-]	5.00	12.0
$C_{L_{\max}}$	Maximum lift coefficient [-]	2.00	2.80
BPR	Bypass ratio [-]	4.00	11.0
Π_{fan}	Fan pressure ratio [-]	1.30	1.70
Π_{lpc}	LPC pressure ratio [-]	1.30	1.70
Π_{hpc}	HPC pressure ratio [-]	10.0	20.0
TET	Turbine entry temperature [K]	1100	1700
h_{cr}	Initial cruise altitude [km]	6.00	12.0
M_{cr}	Cruise Mach number [-]	0.60	0.80

a maximum wing span. For the aircraft category under consideration, this limit is set to 36 m.

The fourth constraint restricts the aircraft lift coefficient in cruise condition due to buffet onset. The lift coefficient at which buffet occurs, for a given sweep angle, is estimated from the buffet onset boundaries provided by Obert [30]. Finally, a constraint is added to limit the maximum achievable lift coefficient. As discussed by Obert, $C_{L_{\max}}$ decreases with increasing quarter-chord wing sweep angle according to a linear relation with the cosine of this angle. A value of 2.8 relates to the maximum lift coefficient attainable at zero sweep angle. The latter two constraints are plotted in Figure 1. Other flight and field performance constraints are considered in the Class I sizing module (Section II.B.1).
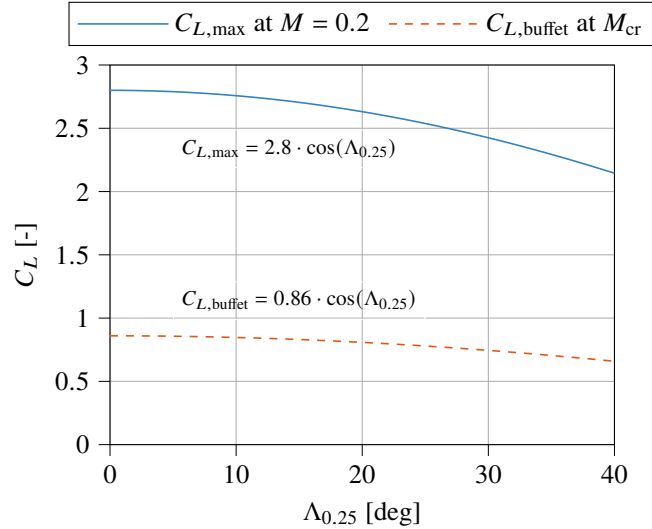
Fig. 1   Constraints on $C_{L_{\max}}$ and $C_{L_{\text{buffet}}}$

The structure of the design and optimization approach is presented in Figure 2 in the format of an extended design structure matrix (XDSM), as introduced by Lambe and Martins [31]. The airframe and propulsion design disciplines

both consist of several design modules as shown in Figures 3 and 4. A multiple discipline feasible (MDF) scheme with Gauss-Seidel procedure is implemented for this problem with limited complexity. The working principles and assumptions of the individual analysis methods on the diagonal of the XDSM are elaborated in the subsequent section. In this framework, the optimizer and converger modules are separated. The inner convergence loop ensures that the airplane, defined by the design variables set by the optimizer, is consistent in terms of operating empty mass and maximum take-off mass.
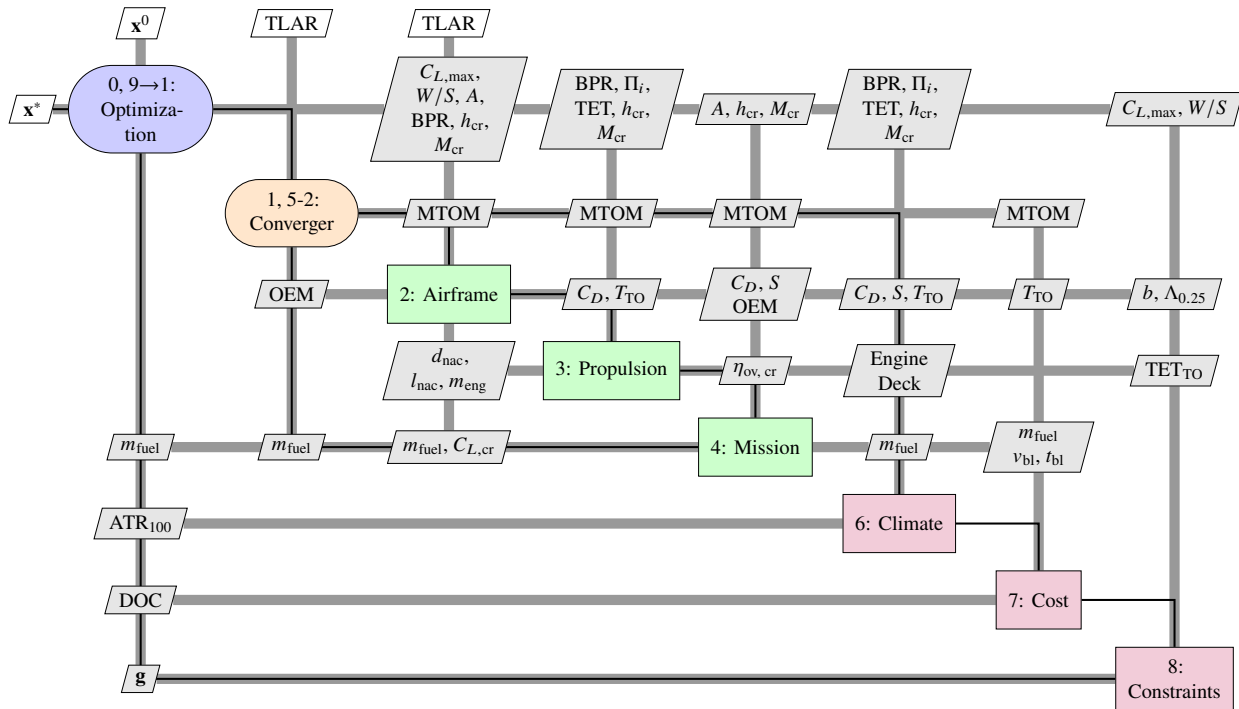
Fig. 2   Extended design structure matrix showing the multidisciplinary design workflow
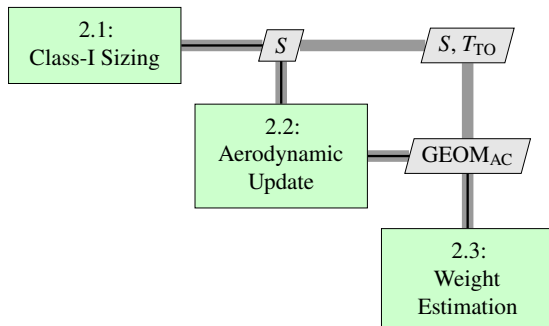

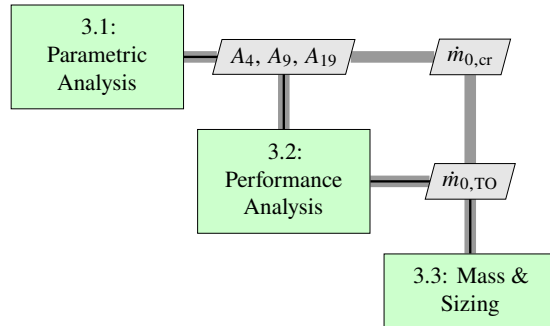**Fig. 3   Airframe design and analysis workflow (step 2 of workflow in Figure 2)**

Fig. 4   Propulsion design and analysis workflow (step 3 of workflow in Figure 2)

B. Analysis Methods

As introduced above, answering the research question requires a multidisciplinary approach to capture interrelated effects of design choices. In this subsection, the methodologies and assumptions of these disciplines are discussed in more detail.

1. Class-I Sizing

Based on the inputs of aspect ratio, wing loading, maximum lift coefficient, cruise altitude and Mach number, a preliminary sizing study is performed to size the wing area (S) and the sea-level take-off thrust (T_{TO}). The sea-level thrust-to-weight ratio is computed as the maximum required for three performance conditions: take-off distance (included through the take-off parameter TOP), cruise Mach number (M_{cr}) at the beginning of cruise, and the second-segment climb gradient (c/V) in one-engine-inoperative condition:

$$\frac{T_{\mathrm{TO}}}{W} = \max\left(\frac{W/S}{\mathrm{TOP}} \frac{1}{C_{L_{\mathrm{TO}}}}, \quad \left(\frac{\rho_0}{\rho_{\mathrm{cr}}}\right)^{\frac{3}{4}} \left[\frac{C_{D_0} \frac{1}{2}\gamma p_{\mathrm{cr}} M_{\mathrm{cr}}^2}{(W/S)_{\mathrm{cr}}} + \frac{(W/S)_{\mathrm{cr}}}{\pi A e \frac{1}{2} p_{\mathrm{cr}} \gamma M_{\mathrm{cr}}^2} \right], \quad \frac{N_{\mathrm{eng}}}{N_{\mathrm{eng}}-1}\left(\frac{c}{V} + 2\sqrt{\frac{C_{D_0}}{\pi A e}} \right) \right) \tag{2}$$

Here, the acronym TOP is the take-off parameter, which correlates to the take-off distance [32]. $C_{L_{\mathrm{TO}}}$ is the take-off lift coefficient, which, in turn is assumed to be related to the maximum lift coefficient according to $C_{L_{\mathrm{TO}}} = C_{L_{\mathrm{max,TO}}}/1.21 = \left(C_{L_{\mathrm{max}}} - 0.3\right)/1.21$. The value of 0.3 is derived from the different take-off and landing flap settings. $(W/S)_{\mathrm{cr}}$ is the wing loading at the start of the cruise phase. Furthermore, C_{D_0} and e are the zero-lift drag coefficient and Oswald factor, respectively. γ is the ratio of specific heats and N_{eng} is the number of engines. ρ_{cr} and p_{cr} are the density and pressure at cruise altitude respectively. These values are dependent on the cruise altitude (h_{cr}), which is a design variable in this study. Hence, the pressure and density in Equation (2) are adapted according to the relations of the International Standard Atmosphere model in Table 2 as a function of the cruise altitude set by the optimizer.

Table 2 **Calculation of temperature, pressure and density as a function of the selected cruise altitude h_{cr} (in meter) according to the International Standard Atmosphere (ISA) model**
($g = 9.81\,\mathrm{m/s^2}$, $R = 287\,\mathrm{J/(kg\,K)}$)

Parameter [Unit]	Troposphere ($0 \le h_{\mathrm{cr}} \le 11\,\mathrm{km}$)	Stratosphere ($11 < h_{\mathrm{cr}} \le 20\,\mathrm{km}$)
Temperature T_{cr} [K]	$288.15 - 0.0065 \cdot h_{\mathrm{cr}}$	216.65
Pressure p_{cr} [N/m^2]	$101325\,(T_{\mathrm{cr}}/288.15)^{-g/(0.0065R)}$	$101325 \cdot e^{-g(h_{\mathrm{cr}}-11000)/(216.65R)}$
Density ρ_{cr} [kg/m^3]	$p_{\mathrm{cr}}/(R \cdot T_{\mathrm{cr}})$	$p_{\mathrm{cr}}/(R \cdot T_{\mathrm{cr}})$

2. Aerodynamics

The aerodynamic module computes the drag polar of the airplane as a function of its geometry. The geometry is influenced directly by the selected design variables, as well as changes in the engine size. The creation of the geometry

is summarized in Appendix C. The aerodynamic discipline provides an update to the estimated drag polar, which, in turn, is employed in the propulsion discipline and mission analysis. Furthermore, this polar is also fed back to the Class-I sizing module to re-evaluate the thrust-to-weight ratio according to Equation (2).

The drag estimation methods are set up according to the to techniques laid out by Obert. The following quadratic drag polar is assumed:

$$C_D = C_{D_0} + \beta \cdot C_L^2 \tag{3}$$

for which two constants have to be computed specific to the design variables. The β constant is dependent on the wing aspect ratio A and the Oswald factor e. Obert proposes the following relation to determine β, based on statistical analysis:

$$\beta = \frac{1}{\pi A e} \approx \frac{1.05}{\pi A} + 0.007 \tag{4}$$

The first term of Equation (3), C_{D_0}, constituting of friction, profile and excrescence drag, is assumed to be independent of the lift coefficient. C_{D_0} can be calculated by adding the sum of the minimum pressure drag of all aircraft components, and the drag contributions due to aircraft size dependent (control surface gaps, doors, etc.) and aircraft size independent (antennas, sensors, etc.) excrescences or protuberances:

$$C_{D_0} = \sum C_{D_{p,\min}} + \Delta C_{D_{E,I}} + \Delta C_{D_{E,II}} \tag{5}$$

$C_{D_{p,\min}}$ of each component is computed according to the flat plate analogy, including shape and compressibility corrections. Aircraft size dependent excrescence drag ($\Delta C_{D_{E,I}}$) is taken to be 1.5% of the total profile drag, $\sum C_{D_{p,\min}}$, assuming hydraulically smooth control surfaces. The size independent contribution ($\Delta C_{D_{E,II}}$) is presumed to be equal to $0.035/S$. To obtain the drag polars in landing and take-off configurations, constant contributions are added to C_{D_0} and e to account for the extension of the flaps and the landing gear. In the take-off configuration, contributions of 0.015 and 0.05 [32] are added to C_{D_0} and e, respectively. In the landing phase, C_{D_0} and e are assumed to be approximately 0.085 and 0.10 higher [32] than the nominal values, respectively.

3. Mass Estimation

To capture the effect of design choices on the operating empty mass (OEM) of the aircraft, a Class-II weight estimation is implemented. The mass estimation is performed according to the methods presented in Appendices C and D of the book by Torenbeek [33]. These semi-empirical and statistical methods allow the prediction of the weight of individual structural groups (i.e. wing, fuselage, empennage, undercarriage and propulsion) as well as the mass of airframe equipment and operational items.

As can be seen from previous research into global warming impact reduction, the wing aspect ratio is increased in

several instances [6, 7, 10, 12] to lower the induced drag. However, this design change can have a dramatic effect on the wing weight, although this penalty may be lessened by increasing the wing thickness and/or decreasing the wing sweep. Although the employed methods are sensitive to the aspect ratio, the result may be inaccurate for high aspect-ratio values since limited or no reference data is available for such slender wings. Therefore, the aspect ratio is limited to 12.

The structural mass of the fuselage is calculated in a similar manner employing a combination of statistical and empirical relationships. However, this mass remains (approximately) constant throughout the optimization since the fuselage geometry is independent of the chosen design variables.

Since the wing geometry and location affects the geometry of the empennage, also the mass of the horizontal and vertical tails is updated throughout the optimizations. This mass prediction is dependent on the respective tail surface and sweep angle. The mass of the undercarriage varies according to the maximum take-off mass of the aircraft, while in all cases it is assumed that the landing gear is retractable and is located in a low-wing configuration.

As will be further elaborated in the next section, the mass of the engines is updated according to the required size (i.e. mass flow), bypass ratio and overall pressure ratio. Also, the impact of high-bypass-ratio engines on nacelle mass is included in the weight assessment of the propulsion group. Furthermore, a forecast of the airframe services and equipment weight is included. The mass of this group is assumed to be equal to a fraction of the maximum take-off mass (MTOM). This fraction is dependent on the aircraft category. For the operating items, a similar approach is taken.

The outcome of this model is fed forward to the propulsion discipline, the mission analysis and in the subsequent aircraft iteration to update the wing surface area. Furthermore, to ensure that a consistent mass is adopted in all design modules, the operating empty mass has to converge to complete the convergence loop (1, 5-2) in the design framework of Figure 2.

4. Propulsion

In the current aircraft configuration, propulsion is provided by two turbofan engines installed on the wing, featuring a two-spool architecture with separate exhausts. Five key design variables are selected for the turbofan cycle, being the bypass ratio (BPR), fan pressure ratio (Π_{fan}), low-pressure compressor ratio (Π_{lpc}), the pressure ratio of the high-pressure compressor (Π_{hpc}) and the total turbine entry temperature (TET). Additional variables required by the discipline are component polytropic efficiencies, mechanical efficiencies, and inlet and combustor pressure losses. These parameters are related to the available technology level and are assumed constant throughout the optimization. Example values of the latter parameters are included in Section V.A for the verification case.

Based on the cruise drag polar and cruise conditions, the thermodynamic cycle is determined by the parametric analysis module of Figure 4. Subsequently, off-design analysis can be carried out to find the required fuel flow for a given thrust at key points in the mission. Both the on-design and off-design point analyses are executed employing the strategies laid out by Mattingly et al. [29], and the variable specific heat model introduced by Walsh and Fletcher [34].

11

Several simplifying assumptions, such as constant component efficiencies are made in the models to limit computational cost and to eliminate the need for component maps in this early design stage. This loss in accuracy is accepted since the verification cases in Section III show limited deviations. Additionally, cooling flows and power extraction are neglected in the current case study for the sake of simplicity.

The results from the thermodynamic analyses are utilized in the third module of the propulsion workflow in Figure 4 to estimate the fan diameter and bare engine mass, which are required by the other disciplines to update the aerodynamic drag and structural masses accordingly. The fan diameter is calculated by assuming an axial Mach number of 0.6 at the fan inlet face and a hub-to-tip ratio of 0.3 for the local cross-section, taking into account the spinner. The mass of a single turbofan engine is estimated using the following relation [35]:

$$m_{\mathrm{eng}}[\mathrm{lbs}] = a \cdot \left(\frac{\dot{m}_{\mathrm{core,TO}}[\mathrm{lb/s}]}{100} \right)^b \cdot \left(\frac{\Pi_{\mathrm{core,TO}}}{40} \right)^c \tag{6}$$

where a, b and c are polynomial functions of the bypass ratio. This formulation, which is based on simulations by the more advanced weight estimation software WATE++, allows to include the weight penalties due to high bypass ratios and pressure ratios, while only a limited number of inputs is required.

As briefly introduced in Section I, the engine design can have a strong effect on the emitted species. While high pressure ratios and temperatures typically lead to reduced fuel consumption and thus low(er) CO_2 emissions, they also increase the production of thermal NO_x [16]. The production of NO_x is also influenced by the detailed combustor design, which is not captured by the current design vector and is out of scope for the current study. From a thermodynamic perspective, the bypass ratio can further improve fuel consumption, although sufficiently high pressure ratios and temperatures are required to power the large fan [5], worsening NO_x emissions. Finally, increased overall propulsive efficiency due to increased bypass ratio or OPR is expected to lead to more frequent contrail formation, possibly at higher ambient temperatures [18] and thus at lower altitudes. Hence, balancing the fuel consumption and CO_2 production against the effects of NO_x and contrails is important.

5. Mission Analysis

The aircraft is sized for a standard design mission for which the mission profile is shown in Figure 5. Reserve fuel is accounted for by including a diversion range to another airport (approximately 460 km or 250 nm) and a loiter phase of 35 minutes. In step 4 of the framework presented in Figure 2, the lost-range method [36] is employed to determine the fuel mass which is required to iterate upon the MTOM and OEM. This method computes the mission-fuel mass ($m_{\mathrm{fuel, mission}}$) to take-off mass ($m_{\mathrm{TO}}$) ratio for the standard mission from the cruise range (r_{cr}), altitude (h_{cr}), lift-to-drag

ratio ($(L/D)_\text{cr}$) and engine overall efficiency ($\eta_\text{ov, cr}$) according to the following equations:

$$\frac{m_\text{fuel, mission}}{m_\text{TO}} = \frac{r_\text{cr}/R_\text{H}}{p + (1/2) \cdot r_\text{cr}/R_\text{H}} + \frac{h_\text{cr, eq}}{0.7 \cdot \eta_\text{ov, cr} \cdot R_\text{H}} + \frac{0.0025}{\eta_\text{ov, cr}}$$

$$\text{where } R_\text{H} = \frac{\text{LHV}}{g}, \quad p = \eta_\text{ov, cr} \cdot \left(\frac{L}{D}\right)_\text{cr}, \quad h_\text{cr, eq} = h_\text{cr} + \frac{v_\text{cr}^2}{2 \cdot g} \tag{7}$$

The three terms in Equation (7) consider different flight phases: the first term determines the fuel spent during the cruise phase. The second part accounts for the fuel required to take off and climb to the cruise altitude, where $h_\text{cr, eq}$ combines the altitude increase and the acceleration to cruise speed. The factor $0.7 \cdot \eta_\text{ov, cr}$ approximates the engine efficiency during the climb phase. The last term adds a minor contribution for maneuvering. Two terms can be included to account for a given diversion range (r_div) and a loiter phase of t_hold hours [36]:

$$\left(\frac{\Delta m_\text{fuel}}{m_\text{fuel, mission}}\right)_\text{div} = 1.20 \cdot \frac{r_\text{div}}{r_\text{harm}} \tag{8}$$

$$\left(\frac{\Delta m_\text{fuel}}{m_\text{fuel, mission}}\right)_\text{hold} = 0.20 \cdot t_\text{hold} \cdot \frac{R_\text{H}}{r_\text{harm}} \cdot \left(1 - \frac{m_\text{fuel, mission}}{m_\text{TO}}\right) \tag{9}$$

In the above equations, r_harm is the harmonic range of the aircraft. This leads to the following estimate of the total fuel mass required for one trip, as a fraction of the take-off mass:

$$\left(\frac{m_\text{fuel}}{m_\text{TO}}\right)_\text{total} = \frac{m_\text{fuel, mission}}{m_\text{TO}} \cdot \left[1 + \left(\frac{\Delta m_\text{fuel}}{m_\text{fuel, mission}}\right)_\text{div} + \left(\frac{\Delta m_\text{fuel}}{m_\text{fuel, mission}}\right)_\text{hold}\right] \tag{10}$$
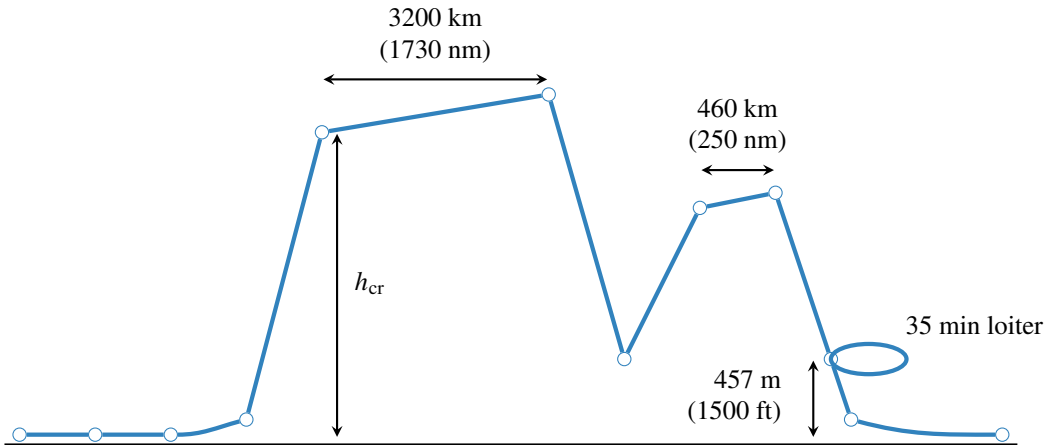

Fig. 5   Mission profile (flown distance versus altitude) under consideration

Together with the MTOM estimation from the previous iteration, the required fuel mass can be calculated. This fuel mass is added to OEM estimation and the payload mass to obtain an updated value for the MTOM. Since this lost-range approach is completely analytical, it can be executed efficiently in the synthesis loop.

However, a more detailed mission analysis is required for the climate impact assessment. This is because the emission index of NO_x depends on the engine pressure ratio, combustor inlet temperature and relative humidity, which vary with the operation conditions. Additionally, the formation of contrails is dependent on the ambient temperature. Also, radiative forcing of these non-CO_2 species is sensitive to the flight altitude.

Therefore, in the climate impact assessment module, the mission is simulated numerically by applying basic flight mechanics rules and by analyzing the engine's off-design performance for discrete time steps. Since this mission assessment approach is more time consuming that the lost-range method, it is only called once in every objective function evaluation rather than in every design iteration.

In the global warming impact evaluation, the accumulated emissions over this design mission and altitude of emission are employed to assess the radiative forcing and the average temperature response. Although this provides insight into the climate burden of the aircraft on this specific mission, it has to be noted that this is not fully representative of an aircraft operated in a more flexible manner in a fleet. Including different missions in the cost and climate assessment is proposed as a recommendation for further research in Section V.

6. Global Warming Impact Evaluation

As briefly introduced in Section I, the assessment of the climate impact of an aircraft is a nontrivial task. Ideally, the societal costs and damages due to emissions would be calculated and compared to operating costs to make a cost-benefit analysis. However, due to large uncertainties, it is almost impossible to evaluate these costs and damages accurately in a conceptual design stage. Therefore, a suitable climate metric has to be selected. To make an insightful evaluation, Grewe and Dahlmann [37] suggested a five-step process to define the impact valuation and avoid misconceptions.

Firstly, the question to be answered has to be clarified. In this study, the objective is to compare the climate impact of aircraft optimized for different objectives (fuel, costs and climate impact). Secondly, the reference aircraft is a non-optimized, yet consistent aircraft design which also serves as a starting point for the optimizations. Thirdly, an emission scenario is to be defined. It is decided to count the emissions over the entire operational lifecycle of a new aircraft to be introduced in 2020. This hypothetical aircraft is assumed to be produced for a period of 30 years, while its operational lifetime is assumed to be 35 years (ignoring potential airframe losses). Accordingly, the maximum fleet size will occur in the years 2050 to 2055. Section IV discusses this fleet scenario definition and productivity constraint in further detail.

Grewe and Dahlmann discuss several climate metrics which are available and their features. In this research, the average temperature response (ATR) is selected as the metric representing global warming impact since it captures the effect of emissions on the surface temperature change (ΔT) while limiting the influence of the time horizon on the result.

The average temperature response is computed as follows for a period of H years:

$$\text{ATR}_H = \frac{1}{H} \int_0^H \Delta T(t) \, dt \tag{11}$$

Note that in this section the time variable t is expressed in years and t_0 represents the initial year of the considered period, e.g. 2020. As a final step of the proposed process, the time horizon H of 100 years is imposed because it provides a balanced assessment between long-lived emissions (CO_2) and more short-lived forcing effects (such as NO_x and contrail formation) [13]. Thus the final metric is ATR_{100}, which requires the computation of ΔT for each year in the selected time horizon. The temperature change can be computed as follows [14, 38]:

$$\Delta T(t) = \int_{t_0}^t G_T(t - t') \cdot \text{RF*}(t') \, dt' \quad \text{with} \quad G_T(t) = \frac{2.246}{36.8} e^{-t/36.8} \tag{12}$$

RF* in Equation (12) is the normalized radiative forcing. This parameter is equal to one for a doubling in atmospheric carbon dioxide concentration compared to pre-industrial times. The actual radiative forcing corresponding to a doubling of this concentration, $\text{RF}_{2 \times CO_2}$, is taken to be $3.7 \, \text{W/m}^2$ [39]. The normalized radiative forcing in Equation (12) is the summed value of several species:

$$\text{RF*}(t) = \sum_i^{\text{all species}} \text{RF*}_i(t) = \sum_i^{\text{all species}} \left[\text{Eff}_i \cdot \frac{\text{RF}_i(t)}{\text{RF}_{2 \times CO_2}} \right] \tag{13}$$

for $i = CO_2$, NO_x-CH_4, NO_x-O_{3L}, NO_x-O_{3S}, H_2O, SO_4, soot and contrails

Eff_i is the efficacy of a given element, which is equal to the ratio between the climate sensitivity of this species and the climate sensitivity of CO_2 [14]. Table 3 provides values for these efficacy and sensitivity parameters. To capture the effects of all these species, a linearised temperature response model is developed (module 6 in Figure 2), based on methods from literature. The subsequent paragraphs elaborate the implemented methods per species which translate the emissions (in kg) into the normalized radiative forcing, and subsequently into the approximate temperature change.

Table 3 **Climate sensitivities (λ_i) and efficacies (Eff_i) for species under consideration [39–41]**

Species	CO_2	CH_4	O_3	H_2O	SO_4	Soot	Contrails
λ_i [K/(W/m^2)]	0.73	0.86	1.00	0.83	0.66	0.51	0.43
Eff_i	1.00	1.18	1.37	1.14	0.90	0.70	0.59

Carbon Dioxide The emission of carbon dioxide is directly related to the combustion of fossil fuels, with an emission index of approximately 3.16 kg/kg for kerosene. Carbon dioxide is a greenhouse gas with a long lifetime which makes

the effects independent of the emission location. An increase in the atmospheric concentration of this species results in a warming effect. The methods introduced by Sausen and Schumann [38] provide a convenient approach to estimate the temperature change due to CO_2 emissions. From the emissions in a given year, the change in atmospheric CO_2 concentration, denoted by $\Delta\chi_{CO_2}$, can be computed. This change is given by the following convolution integral:

$$\Delta\chi_{CO_2}(t) = \int_{t_0}^{t} G_{\chi_{CO_2}}(t - t') \cdot E_{CO_2}(t') \, dt' \quad \text{with} \quad G_{\chi_{CO_2}}(t) = \sum_{i=1}^{5} \alpha_i \cdot e^{-t/\tau_i} \tag{14}$$

where E_{CO_2} represents the absolute CO_2 emissions (in kg or Tg) in year t. Table 4 provides the α_i coefficients and perturbation lifetimes τ_i for the impulse response function $G_{\chi_{CO_2}}$. If the concentration change $\Delta\chi_{CO_2}$ is known, the normalized radiative forcing can be obtained from the ratio between the updated concentration and the background concentration, $\chi_{CO_2,0}$, which is assumed to be equal to 380 ppmv:

$$RF^*(t) = \frac{1}{\ln 2} \cdot \ln\left(\frac{\chi_{CO_2,0} + \Delta\chi_{CO_2}(t)}{\chi_{CO_2,0}}\right) \tag{15}$$

Table 4   Coefficients of impulse response function $G_{\chi_{CO_2}}$ in Equation (14) [38]

i	1	2	3	4	5
α_i	0.067	0.1135	0.152	0.0970	0.041
τ_i	∞	313.8	79.8	18.8	1.7

Nitrogen Oxides   Although NO_x is not a greenhouse gas itself, it causes several indirect effects which are expected to have a net warming effect [1, 42]. However, unlike carbon dioxide, the emission index is not constant but rather dependent on the engine operating condition and combustor technology. There are several options to approximate the emission index, either through an analytical expression [5, 7] or through fuel-flow methods [13]. In this research, the analytical expression from Schwartz Dallara [43] is employed:

$$EI_{NO_x} = 0.0986 \cdot \left(\frac{p_{T3}}{101325}\right)^{0.4} - e^{T_{T3}/194.4 - H_0/53.2} \tag{16}$$

where p_{T3} and T_{T3} are the pressure and temperature ahead of the engine combustor, and H_0 is specific humidity. This expression can be evaluated at every point in the mission profile from an off-design analysis of the turbofan engine, and provides the actual emission of NO_x through multiplication with the fuel flow $\dot{m}_{fuel}$.

On a long-term basis, NO_x depletes atmospheric methane (CH_4) and long-lived ozone (O_{3L}), which are both greenhouse gases. The depletion of these agents results in a cooling effect. The radiative forcing of these effects can be

modeled according to [41]:

$$\mathrm{RF}_i(t, h) = s_i\,(h) \int_{t_0}^{t} G_i\,(t - t') \cdot E_{\mathrm{NO_x}}\,(t')\,dt' \quad \text{with} \quad G_i\,(t) = A_i \cdot \mathrm{e}^{-t/\tau_i} \quad \text{for } \mathrm{i} = \mathrm{CH_4}, \mathrm{O_{3L}} \tag{17}$$

In this equation, the coefficient A_i is assumed to be equal to -5.16×10^{-13} (W/m^2) / kg$_{\mathrm{NO_x}}$ and -1.21×10^{-13} (W/m^2) / kg$_{\mathrm{NO_x}}$ for methane and long-lived ozone, respectively. The perturbation lifetime τ_n is set to 12 years. $s_i\,(h)$ is a forcing factor, as defined in Ref. [41], to account for the altitude variation of $\mathrm{NO_x}$ and contrail effects.

The most prominent warming effect of $\mathrm{NO_x}$ emissions is the formation of short-lived ozone in the troposphere and lower stratosphere. Since this is a short-lived effect, no convolution integral with response function is required, but a simpler method can be applied:

$$\mathrm{RF}_{\mathrm{NO_x\text{-}O_{3S}}}(t, h) = s_{\mathrm{NO_x\text{-}O_{3S}}}\,(h) \cdot \left(\frac{\mathrm{RF}_{\mathrm{ref}}}{E_{\mathrm{ref}}}\right)_{\mathrm{NO_x\text{-}O_{3S}}} \cdot E_{\mathrm{NO_x}}(t) \tag{18}$$

Similar to Equation (17), also here a forcing factor $s(h)$ is included to simulate the altitude dependency of the radiative effects. The constant $\mathrm{RF}_{\mathrm{ref}}/E_{\mathrm{ref}}$ represents the radiative forcing due to $\mathrm{NO_x}$-$\mathrm{O_{3S}}$ per unit of $\mathrm{NO_x}$ emission. It is assumed to be equal to 1.01×10^{-11} (W/m^2) / kg$_{\mathrm{NO_x}}$, although a large uncertainty is present.

This assessment of $\mathrm{NO_x}$ depends on certain simplifying assumptions. Firstly, the changing lifetime of methane, due to its depletion, is not taken into account [44]. This can be considered a steady-state assumption. Finally, while also the geographic location of emissions performs a role, it is not taken into account in this analysis.

Water, Soot and Sulfate   In the combustion process, also other short-lived species are formed such as water vapor, and aerosols such as soot (black carbon) and sulfate. To compute the absolute emissions of these species, constant emission indices are assumed: $\mathrm{EI}_{\mathrm{H_2O}} = 1.26$ kg/kg, $\mathrm{EI}_{\mathrm{soot}} = 2.0 \times 10^{-4}$ kg/kg and $\mathrm{EI}_{\mathrm{SO_4}} = 4.0 \times 10^{-5}$ kg/kg [41]. The impact of these species is modeled in a similar manner to the short-lived ozone production discussed above. However, for these species the altitude dependency factor is omitted, resulting in the following relation [41]:

$$\mathrm{RF}_i(t) = \left(\frac{\mathrm{RF}_{\mathrm{ref}}}{E_{\mathrm{ref}}}\right)_i \cdot E_i(t) \quad \text{for } i = \mathrm{Soot}, \mathrm{H_2O}, \mathrm{SO_4} \tag{19}$$

Contrails   Because the jet exhaust of the turbofan engines is hot and humid compared to the ambient air, condensation trails may form behind an aircraft. Whether or not contrails indeed develop, can be assessed with the help of the Schmidt-Appleman criterion [18]. This criterion is met if the hot exhaust air reaches saturation with respect to liquid water during the mixing process with the surrounding air. The mixing process is modeled by a mixing line in a diagram of water vapor partial pressure versus ambient temperature. This mixing line can be approximated by a linear relationship which depends on the ambient conditions (pressure, temperature and relative humidity), overall engine

efficiency and the emission index of water.

Additionally, the formation can only occur when the static ambient temperature lies below the temperature threshold of 235 K (-38 $^\circ C$). These conditions are not sufficient to ensure that the contrails are persistent. For this to occur, the partial pressure of the mixed exhaust, which has reached the ambient temperature, should lie in between the thresholds for saturation above liquid water and the saturation level above ice. The formulae provided by Sonntag [45] specify these levels as a function of temperature.

These three criteria are evaluated at every point in the mission analysis, using the international standard atmosphere model to obtain the ambient conditions. The selected cruise altitude and engine design variables are expected to influence the outcome. If all three criteria are met, then that point is marked as a time interval in which persistent contrails appear. At the end of the mission analysis, the total contrail length (in km or nm) is used to estimate the radiative forcing according to [41]:

$$\text{RF}_{\text{contrails}}(t, h) = s_{\text{contrails}}(h) \cdot \left(\frac{\text{RF}_{\text{ref}}}{L_{\text{ref}}}\right)_{\text{contrails}} \cdot L(t) \tag{20}$$

where $s_{\text{contrails}}(h)$ is an altitude-dependent forcing factor, $\left(\frac{\text{RF}_{\text{ref}}}{L_{\text{ref}}}\right)_{\text{contrails}}$ is set to 1.82×10^{-12} (W/m^2)/km [2], and $L(t)$ is the accumulated contrail length in year t.

It has to be recognized that the contrail assessment method presented in this section is simplified and that uncertainties remain. Although the results are sensitive to changes in flight altitude and technology variables, the fact that atmospheric conditions may vary regionally or temporally is not accounted for. Additionally, the dependency of the radiative effects on the geographic location is neglected. Finally, only the impact of linear contrails is analyzed. The formation and effects of contrail cirrus are not considered.

7. Operating Costs

Although the fuel costs constitute a large portion of an aircraft's operating costs, other contributions play an important role as well. Reducing the block time (t_{bl}) by increasing the flight speed, for example, decreases the crew costs but may lead to higher fuel costs. Module 7 of Figure 2 employs the methods presented by Roskam [46, Chapter 5] to estimate the cash operating costs for a particular aircraft design (USD/(seat $\cdot$ nm) or USD/(seat $\cdot$ km)) or for a complete fleet (in USD).

Two main contributions are included in the analysis. Firstly, the costs related to flight itself are estimated. These comprise of fuel and oil costs, crew salaries and insurance. A fuel price of 1.78 USD/US gallon is assumed, which is approximately equal to the price level in January 2020 before the influence of the Corona pandemic. The following

relation determines the fuel and oil costs per seat $\cdot$ nm:

$$C_{\text{fuel}} = \frac{m_{\text{f,bl}}}{r_{\text{bl}} \cdot N_{\text{pax}}} \cdot \frac{C_{\text{f,gal}}}{\rho_{\text{fuel}}} \tag{21}$$

$$C_{\text{oil}} = \frac{m_{\text{oil}}}{r_{\text{bl}} \cdot N_{\text{pax}}} \cdot \frac{C_{\text{oil,gal}}}{\rho_{\text{oil}}} = \frac{0.7 \cdot N_{\text{eng}} \cdot t_{\text{bl}}}{r_{\text{bl}} \cdot N_{\text{pax}}} \cdot \frac{C_{\text{oil,gal}}}{\rho_{\text{oil}}} \tag{22}$$

Captain, first officer and flight attendant salaries are also adapted to 2020 levels. It is assumed that each crew member flies 1000 hours annually and that at least 1 cabin crew member is present for each 50 passengers. The cost of a single crew member, expressed in (USD/seat $\cdot$ nm), is defined as follows [46]:

$$C_{\text{crew member}} = \frac{1}{N_{\text{pax}} \cdot v_{\text{bl}}} \cdot \left[(1 + k_j) \cdot \frac{\text{sal}_{\text{crew member}}}{\text{ah}_{\text{crew member}}} + t_{\text{ef}} \right] \tag{23}$$

The parameters in the above equation are explained and quantified in Table 5. The annual hull insurance rate (in USD/USD/airplane/year) is taken to be 0.02.

Table 5   Parameters related to the cost estimation of the flight crew

Parameter [Unit]	Symbol	Value
Factor for employer costs [-]	k_j	0.26 [46]
Annual captain salary [USD/year]	$\text{sal}_{\text{captain}}$	277000 *
Annual first officer salary [USD/year]	$\text{sal}_{\text{first officer}}$	188000 *
Annual cabin crew member salary [USD/year]	$\text{sal}_{\text{cabin crew}}$	43160 †
Annual flight hours [hr/year]	ah	1000 *
Travel expense factor [USD/hr]	t_{ef}	9 [46]

Secondly, the cost of maintenance ($C_{\text{maintenance}}$) is accounted for through the methods introduced in Section 5.2.2 of Reference [46]. This category includes the labor rates of airframe and engine engineers (2020 averaged salaries), as well the cost for airframe and engine spares. The latter two aspects require an appreciation of the aircraft and turbofan engine unit purchase prices. New relations are derived to estimate these prices, based on the aircraft OEM and the single engine static take-off thrust, from recent price figures [47, 48]:

$$P_{\text{AC,2020}}[2020\ \text{USD}] = 0.0052 \cdot \text{OEM}^{0.927} \cdot 10^6 \tag{24}$$

$$P_{\text{eng,2020}}[2020\ \text{USD}] = 0.1604 \cdot T_{\text{TO,eng}}^{0.878} \cdot 10^6 \tag{25}$$

The values of OEM and $T_{\text{TO,eng}}$ in these relations are expressed in kg and kN, respectively. Other cost contributions, such as depreciation and fees related to financing and operations are excluded from the analysis. The reason for this

---

exclusion is that these categories are thought to carry more uncertainty and that they may be dependent on business decisions. For example, the financing cost may depend on the decision whether to buy or lease the aircraft. Additionally, indirect operating costs, such as passenger services, station operation, promotion and administration, are neglected in the current analysis.

In Module 7 of Figure 2, firstly the direct operating costs of one aircraft are calculated. However, since the climate impact is determined for an operating fleet, for a prolonged period of time, it is of interest to express the costs in a similar manner. Knowing the operating cost of one aircraft per year ($C_{\text{ops,AC}}$), the total fleet operating costs $C_{\text{ops,fleet}}$ can be computed as follows:

$$C_{\text{ops,fleet}} = C_{\text{ops,AC}} \cdot \text{RPK}_{\text{AC,ann}} \cdot N_{\text{yr}} \cdot N_{\text{AC}} \tag{26}$$

$$= (C_{\text{fuel}} + C_{\text{oil}} + C_{\text{crew}} + C_{\text{insurance}} + C_{\text{maintenance}}) \cdot \text{RPK}_{\text{AC,ann}} \cdot N_{\text{yr}} \cdot N_{\text{AC}} \tag{27}$$

where $\text{RPK}_{\text{AC,ann}}$ is the amount of revenue passenger kilometers flown by one aircraft in one year, N_{yr} is the operational life of an aircraft, and N_{AC} is the total number of aircraft in the fleet. Values for the latter parameters may vary between objectives due to a difference in block time and thus productivity. Section IV.A discusses this aspect in further detail and introduces the hypothetical fleet scenario.

III. Verification of Analysis Methods

This chapter verifies whether the methods described above work correctly, and whether the overall methodology results in a realistic case study. Special attention is paid to the physics-based propulsion discipline in Section III.A since an accurate estimation of the engine parameters is required to predict the emissions in the climate impact evaluation module. In Section III.B, two aircraft are designed for the same top-level requirements as the Airbus A320-200 and Boeing 777-200 to confirm that the implemented approach allows producing a realistic conceptual aircraft design.

A. Turbofan Performance Verification

The verification of the propulsion discipline consists of two steps: firstly, the design and off-design analyses produced by the implemented methods are compared to a model of the GE90 in the GSP gas turbine simulation program. Secondly, a performance map for varying Mach numbers and altitudes is constructed and compared to GE90 performance data provided by Nicolai and Carichner [49]. The inputs employed to model the GE90 engine are provided in Appendix A.

Table 6 presents the results of the first verification step. The subscripts indicate the engine stations according to ARP 755A station numbering standard. While both the implemented method and GSP model employ the same inputs, the GSP model also includes component maps which provide component efficiency updates according to the operating condition. It can be concluded that the errors between the two models are relatively small and that simplified methods

provide sufficient accuracy. A study of the errors in the design point analysis indicates that these can be attributed to minor differences in the variable specific heat models.

Table 6   Verification of the performance analysis with the implemented methods versus GSP (conditions according to Table 12, gray numbers represent input values)

Parameter [Unit]	Design (Cruise)			Off-design (Take-off)		
	Framework	GSP	Diff. [%]	Framework	GSP	Diff. [%]
T_{T3} [K]	772	771	+0.09	896	897	-0.13
p_{T3} [Pa]	1.42	1.42	+0.04	3.46	3.47	-0.37
T_{T4} [10^3 K]	1.43	1.43	0	1.65	1.66	-0.69
p_{T4} [Pa]	1.35	1.35	+0.04	3.29	3.30	-0.38
$\dot{m}_0$ [10^3 kg/s]	0.557	0.558	-0.17	1.30	1.29	+0.45
$\dot{m}_{\text{fuel}}$ [kg/s]	1.16	1.14	+1.37	3.10	3.10	-0.05
TSFC [kg/(N s)]	1.49×10^{-5}	1.46×10^{-5}	+1.75	8.22×10^{-6}	8.22×10^{-6}	-0.05
N1 [%]	100	100	0	106	103	+3.12
N2 [%]	100	100	0	107	106	+0.86

Secondly, an engine deck of the GE90 is created and compared to data provided in Appendix J of Nicolai and Carichner [49]. The results are presented in Figures 6 and 7 for the net thrust and fuel flow. The values are normalized with respect to the sea-level-static (SLS) values since absolute differences may occur because it is unclear for which exact GE90 type the data is provided. From these figures it can be observed that the thrust and fuel flow values correspond rather well for varying altitude and Mach number, considering the simplifying assumptions discussed above.
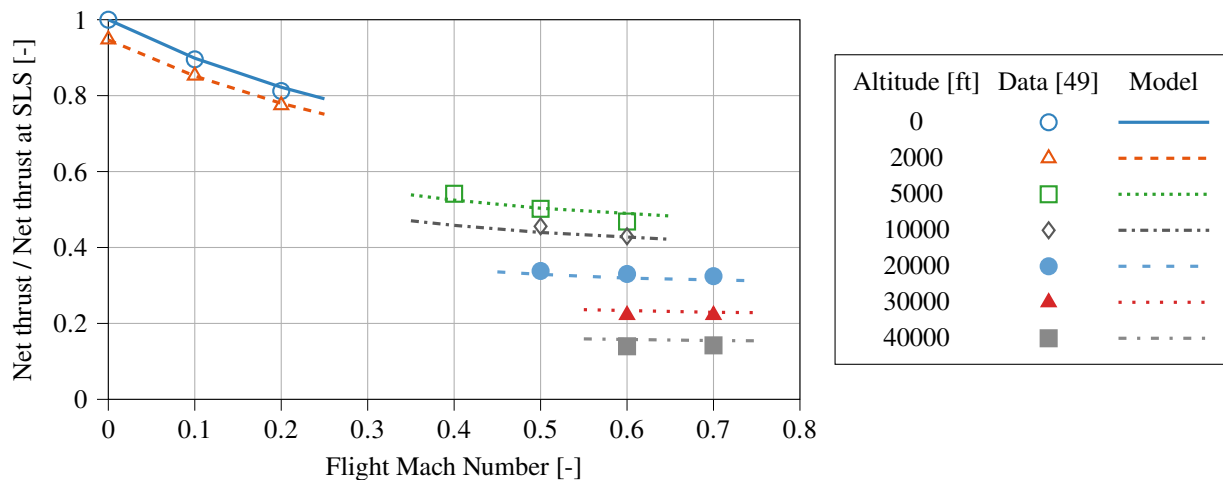

Fig. 6   Validation of maximum net thrust calculation throughout the flight envelope, compared to GE90 engine data [49, Appendix J]
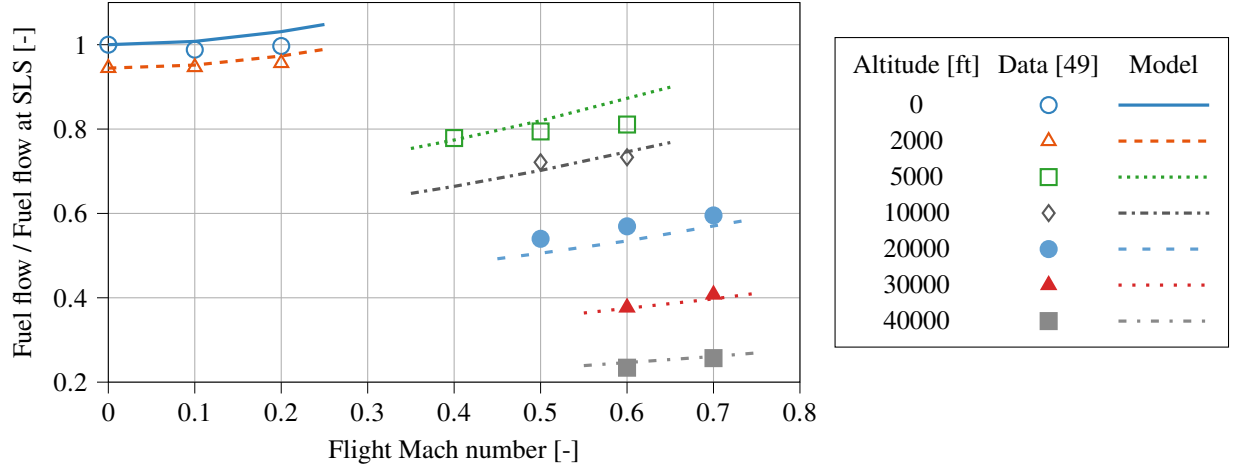
Fig. 7   Validation of fuel mass flow at maximum net thrust calculation throughout the flight envelope, compared to GE90 engine data [49, Appendix J]

B. Aircraft Synthesis Verification

This section discusses the validity of the aircraft design methods and synthesis loop introduced in Section II. The comparison between existing aircraft data and the simulated models is based on three aspects: the mass estimation, the geometry creation and performance evaluation. These aspects are considered for two aircraft, namely the Airbus A320-200 and the Boeing 777-200, representing the narrow-body and wide-body categories. Input values for these two aircraft are included in Appendix B.

Firstly, Table 7 presents the mass estimation obtained with the framework and also compares four key geometric dimensions for both aircraft. These results are obtained after six iterations in the inner convergence loop of the methodology Figure 2. The relative differences for these parameters lie between to -1.6% and +2.5%, which is considered acceptable given the conceptual design level and the simplifying assumptions made in the methodology.

Table 7   Validation of aircraft design modules with Airbus A320-200 and 777-200 [50] (the fuel mass is evaluated at the harmonic range with maximum structural payload)

Parameter [Unit]	Airbus A320-200			Boeing 777-200		
	Framework	Reference	Diff. [%]	Framework	Reference	Diff. [%]
MTOM [metric tons]	72.3	73.5	-1.6	242	243	-0.5
OEM [metric tons]	40.7	41.3	-1.5	134	136	-1.4
Fuel Mass [metric tons]	13.3	13.5	-1.2	52.3	52.2	+0.3
Wing area S [m^2]	126	122	+2.5	437	428	+2.1
Wing span b [m]	34.5	34.1	+1.3	61.6	60.9	+1.2
Fuselage outer diameter d_{fus} [m]	3.96	3.95	+0.2	6.14	6.20	-1.0
Fuselage length l_{fus} [m]	38.2	37.6	+1.8	62.6	62.8	-0.3

Secondly, Figure 8 shows the resulting geometry predictions and the overlap with the actual top view of the aircraft.

Although the computational models agree relatively well with the actual planform, two aspects can potentially be further improved. Firstly, the wing taper ratio is overestimated for both cases. This is because the statistical relation, which relates the taper ratio to the wing sweep, produces an averaged value for various aircraft. For example, it underestimates the taper for a Boeing 737-700. Therefore, it is decided not to correct this relation for the aircraft presented here. Also, the main wing of the Airbus A320-200 is placed slightly more aft than expected. Again, this can be attributed to averaged statistical values, in this case, the location of the aircraft center of gravity (cg) at OEM with respect to the mean aerodynamic chord ($\xi_{cg, OEM} = 0.25$ MAC), and the relative location of the horizontal tail to the fuselage length ($x_{ht}/l_{fus} = 0.91$). The geometry creation is discussed more elaborately in Section V.C.
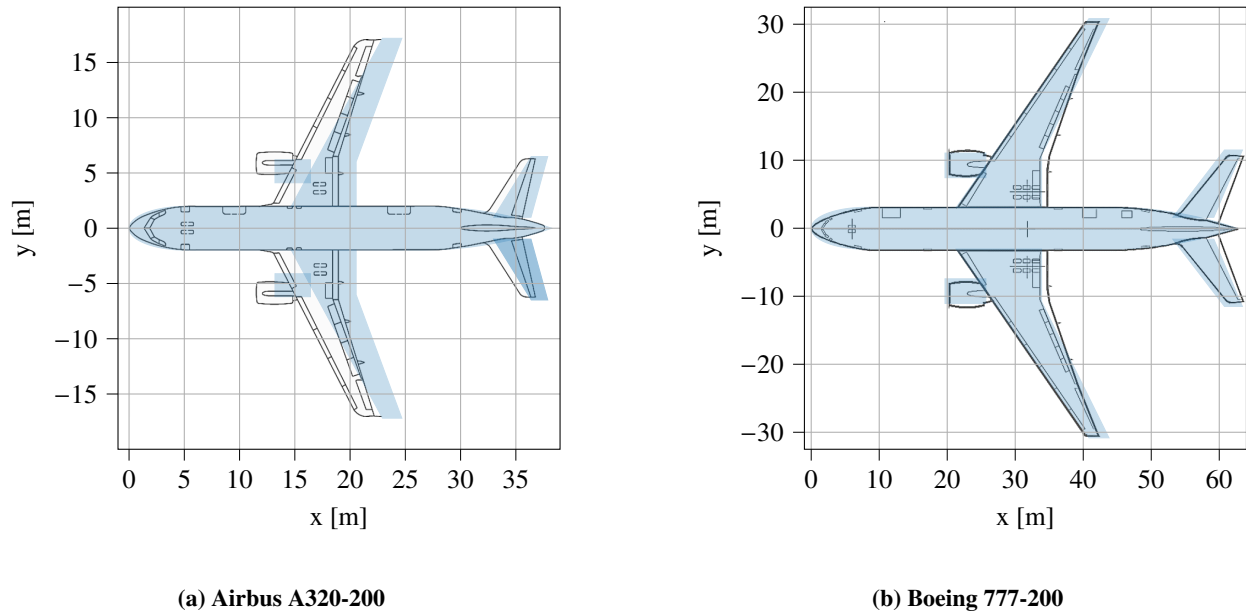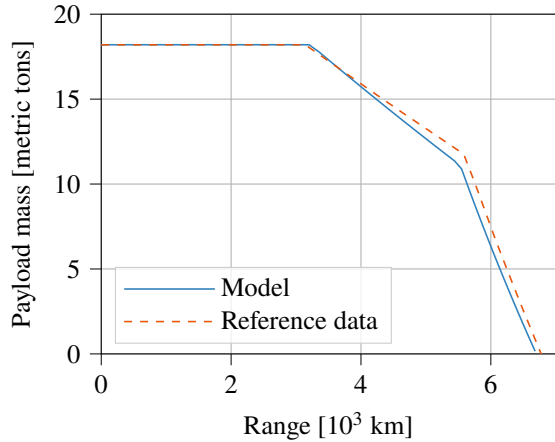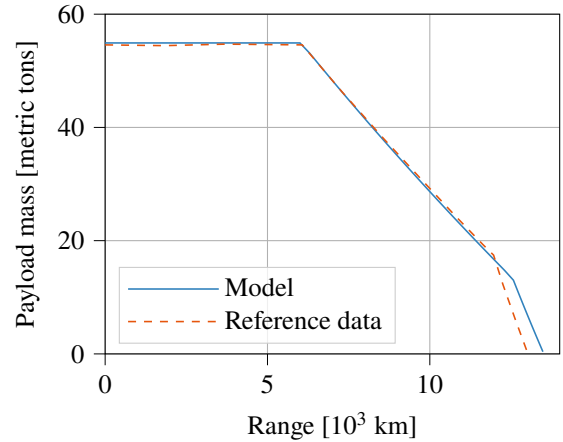

(a) Airbus A320-200

(b) Boeing 777-200

Fig. 8   Comparison between the top view created by the MDO framework (light blue) and the actual geometry (dark lines) [51, 52]

Finally, to verify whether the aircraft performance is evaluated adequately, the payload-range diagrams of the aircraft are compared in Figure 9 with data from aircraft characteristics documents. Also, for the performance aspect, good agreement is achieved with the relatively simple methodology. For the Airbus A320, the slope of the line between the harmonic mission and full fuel tanks is marginally underestimated, which is possibly caused by an underestimation of the engine efficiency or lift-to-drag ratio in the cruise segment. This approximation of this slope is better for the Boeing 777, although the range at maximum fuel capacity is somewhat overestimated.

(a) Airbus A320-200 (M_{cr}=0.78, h_{cr}=11.3 km)   (b) Boeing 777-200 (M_{cr}=0.84, h_{cr}=11.9 km)

**Fig. 9   Comparison between payload-range diagrams obtained with the MDO framework (blue lines)
and the reference diagrams (dashed orange lines) [51, 52]**

IV. Results

Employing the verified methodology from Section II, a commercial aircraft design is optimized for a given set of
top-level requirements. This section presents the results of a series of optimizations and discusses the rationale behind
the design results. We carried out optimizations for three objectives: the climate impact (ATR_{100}), the fleet-wide fuel
mass ($m_{fuel,fleet}$) and operating costs ($C_{ops,fleet}$) by varying the ten design variables introduced in Table 1.

Table 8 presents the top-level requirements which are used throughout all optimization studies. These requirements
correspond to a narrow-body, medium-range aircraft, comparable to the Airbus A320 or Boeing 737. The specified
structural payload represents a high-density cabin layout of 180 passengers in economy class seats, resulting in a
maximum structural payload of approximately 18 metric tonnes.

Table 8   Top-level aircraft requirements employed for the aircraft optimization

Requirement [Unit]	Value
Maximum structural payload [metric tons]	18.2
Harmonic range [km (nm)]	3200 (1730)
Approach speed [m/s (kts)]	70.0 (136)
Take-off length (ISA conditions) [m (ft)]	2100 (6890)

Since previous studies [7, 13] revealed that climate-optimized aircraft tend to fly slower, with an increased block
time as result, it is of interest to study whether such an aircraft can maintain the same productivity level. To gain further
insight in this matter, the hypothetical fleet scenario includes a productivity constraint, as introduced in Section IV.A.
Subsequently, Section IV.B present the optimization results. The optimization strategy is elaborated upon separately in
Section VI.

A. Future Fleet Scenario Definition

Since the climate impact is calculated from an emission scenario over 100 years, the outcome is dependent on the number of flights taking place in this period, and thus the number of active aircraft. Assuming all aircraft in the hypothetical fleet execute only one fixed mission, the number of flights in a given year (year i) is computed from the number of aircraft available in that year, the block time t_{bl} of that mission and the annual utilization U_{ann} of the aircraft type:

$$N_{\text{flights, year i}} = N_{\text{AC, year i}} \cdot \frac{U_{ann}}{t_{bl}} \tag{28}$$

We assume a constant annual utilization, equal to 3700 hours per year for the narrow-body aircraft category studied here. This value follows from statistical analysis of fifteen US based airlines from 1995 to 2019 [53]. The chosen mission largely determines the block time. In this research, the three objectives are evaluated for a fixed mission with $N_{pax} = 130$ passengers (i.e. 13 metric tons of payload) and a stage length r_{bl} of 1852 km or 1000 nm. Research by Husemann et al. [54] indicates that narrow-body aircraft often operate near this payload-range combination.

Additionally, the block time varies with the cruise speed and is thus different for the three objectives, as shown in the subsequent section. Since the varying block time affects the productivity of an aircraft (i.e. number of passenger-kilometers flown in a given time frame), the number of aircraft is not constant, but rather the required productivity in the year 2050. This productivity level is equal for all three objectives under consideration. The imposed level is estimated from passenger transport statistics in the United States for fifteen airlines [53], considering an annual growth of 3% in this region [3]. Hence, this aircraft fleet has to reach a productivity level of approximately 3.95×10^{12} revenue passenger kilometer ($RPK_{\text{fleet,2050}}$) each year in the period from 2050 to 2055.

By imposing this constraint, also the total number of flights carried out each year is equal for the three objectives. In this case, the maximum number of aircraft to be produced, and the number of aircraft active in the period from 2050 to 2055, is provided by the following relation:

$$\begin{aligned} N_{\text{AC, 2050}} &= \frac{RPK_{\text{fleet, 2050}}}{N_{pax} \cdot r_{bl}} \cdot \frac{t_{bl}}{U_{ann}} \\ &= \frac{3.95 \cdot 10^{12}}{130 \cdot 1852} \cdot \frac{t_{bl}}{3700} \end{aligned} \tag{29}$$

The production of the new, hypothetical aircraft starts in 2020, and continues for 30 years. Each aircraft has a lifetime of 35 years, assuming no hull losses occur. The aircraft concept is thus in operation for a period of 65 years. Figure 10 clarifies the scenario construction by presenting the total fleet size and the number of flights for each year in the period of 100 years considered for the climate impact evaluation. The following section discusses the differences between the objectives.
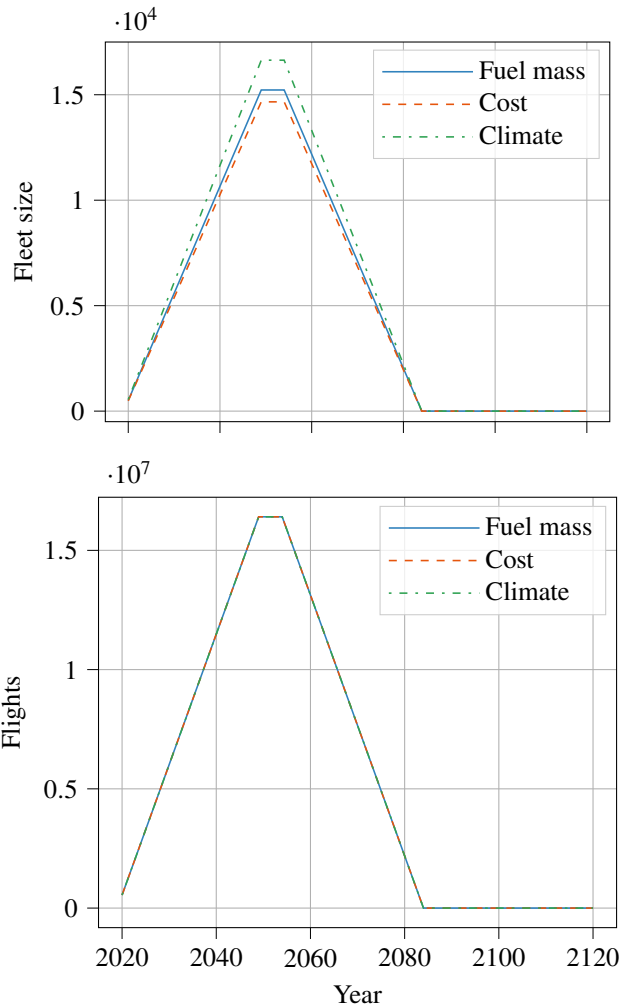
Fig. 10 Future amount of aircraft in operation and number of flights in the hypothetical scenario

B. Single-Objective Optimization Results

Table 9 presents the results of the optimizations for the three objectives introduced at the start of this section. On the left-hand side of the table, the absolute values of the parameters are provided for each optimized objective. The right-hand side shows the relative changes with respect to the minimum achievable value. For example, when an aircraft is optimized for ATR_{100}, the operating costs lie 8.2% above the minimum cost achievable, and the fuel burn is 6.6% higher than the minimum fuel mass found.

The results indicate that none of the three objectives leads to the exact same solution. Although the fuel- and cost-optimized aircraft are rather similar, they appear to be conflicting with the global warming objective. Indeed, even by combining airframe, engine and mission variables, it seems that the climate-optimized solution does not correspond to the minimum fuel burn solution and that operating costs are increased. Tables 10 and 11 show the selected design variables and other performance indicators, respectively, to shed a light on the design choices made for each individual

Table 9   Optimized objective values (denoted by *) and relative differences

Objective	Absolute values			Relative to minimum value		
	$m_{\textbf{fuel}}$ [10^{11} kg]	$C_{\textbf{ops}}$ [10^{13} USD]	$\textbf{ATR}_{100}$ [mK]	$m_{\textbf{fuel}}$	$C_{\textbf{ops}}$	$\textbf{ATR}_{100}$
Fuel mass	1.19*	9.87	26.8	-	+2.6%	+128%
Cost	1.26	9.62*	27.0	+6.1%	-	+130%
Climate	1.27	10.4	11.8*	+6.6%	+8.2%	-

design objective. The resulting top views of the optimized aircraft are displayed in Figure 11.

In the case of the fuel mass objective, it is clear that the optimizer moves to a design point with high aspect ratio for reduced lift induced drag. Furthermore, the overall pressure ratio (OPR) of 56.7 approaches the highest value allowed within the specified bounds. The bypass ratio of 9.0 is relatively high, but not maximized. This may be due to a trade-off with installation effects, and because the allowable turbine entry temperature in take-off conditions is limited. These design changes result in an optimal fuel consumption of approximately 5200 kg per flight.

Table 10   Optimized design variables for the three design objectives considered

Variable [Unit]	Fuel Mass	COC	ATR_{100}
W/S [kN/m^2]	6.03	5.55	6.08
A [-]	11.6	9.05	12.0
C_{L_max} [-]	2.69	2.60	2.80
BPR [-]	9.00	7.12	10.5
Π_fan [-]	1.59	1.80	1.40
Π_lpc [-]	1.80	1.42	1.37
Π_hpc [-]	19.8	20.0	19.5
TET [10^3 K]	1.52	1.55	1.45
h_cr [km]	10.1	10.2	7.56
M_cr [-]	0.708	0.751	0.600

The design of the aircraft with minimized operating costs (approximately 0.129 USD$_{2020}$/(seat · nm)) appears to be driven by the block time, which is the shortest of the optimized aircraft as can be seen in Table 11. This parameter, and its related block speed, play an important role in the labor costs of the crew and maintenance technicians, since these costs are related to the flight hours. Although the fuel costs perform an important role in cost minimization, they are not dominant. Nevertheless, the relative contribution depends on the fuel price, which is assumed to be 1.78 USD/US gallon in this study. Higher fuel prices for given labor rates can make the design more sensitive to the fuel burn. Ideally, the aircraft would fly at an even higher Mach number to reduce labor costs further. Nonetheless, this is hindered by the constraint on the maximum lift coefficient, which decreases with increased sweep and thus cruise speed.
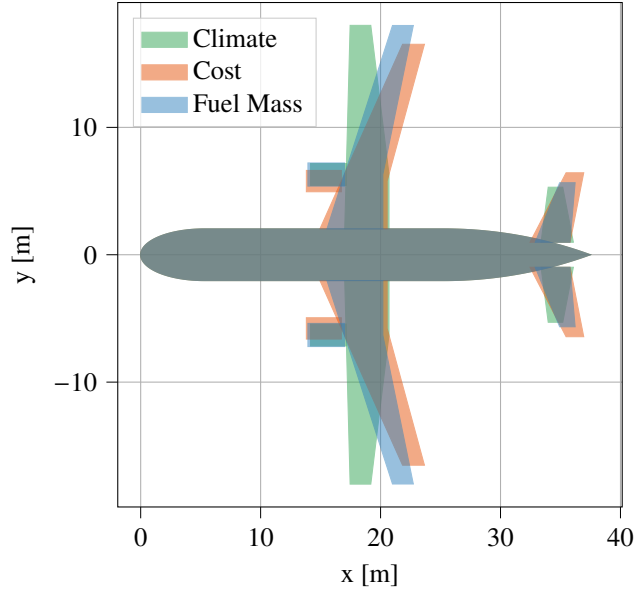
Fig. 11 Top view of aircraft optimized for three different objectives

Additionally, since this $C_{L,\max}$ constraint appears to be active for all objectives, the variable can be removed from the design vector in future optimization studies with the current framework. $C_{L,\max}$ can rather be calculated directly from the quarter-chord sweep angle, which in turn follows from the selected cruise Mach number.

The climate-optimized aircraft, however, exhibits a different design. The average temperature response also takes the short-lived climate agents into account, of which NO_x and contrails are prevalent and have an altitude dependency. It can be seen in Table 10 that the optimal cruise altitude is considerably lower than the fuel-optimized and cost-optimized aircraft, i.e. 7.56 kilometers vs. 10.1 km. This can be explained as follows: in the case of NO_x, this reduces the radiative forcing due to the creation of short-lived ozone [55]. For contrails, flying lower reduces the probability of contrail formation due to the higher ambient temperatures. These two effects are reinforced by the choice of engine design variables: the lower design OPR (37.4 compared to 56.7 for the fuel-mass objective) reduces the emission index of NO_x and decreases the overall engine efficiency (29.5% compared to 32.7% for the fuel-mass objective). The latter aspect reduces the slope of the mixing line in the Schmidt-Appleman criterion, lowering the probability of persistent contrail formation further. It can be argued that this also reduces the climate impact due to contrail cirrus, although this is not considered in the optimizations.

Furthermore, it is observed that the aircraft operates at a significantly lower Mach number of 0.60, at the lower bound of this variable. It is expected that two reasons lead to this result: first, the cruise speed has to be adapted to the lower altitude to achieve the optimal lift-to-drag ratio in cruise. Secondly, the lower Mach number does not require a (large) sweep angle and allows for larger thickness-to-chord ratios, both reducing the structural mass of the wing. To better suit the operation at such low Mach numbers, it would of interest to study exchanging the turbofan cycle for a

propeller-based propulsion system.

Although the engine efficiency of the climate-optimized aircraft is reduced, the data in Table 11 indicates that the thrust specific fuel consumption is slightly lower compared to the fuel- and cost-optimized aircraft. This may appear to be contradictory. Nevertheless, it is correct that the efficiency of the climate-optimized aircraft is lower, not only due to the decrease in overall pressure ratio, but also because of the lower cruise speed. The latter design choice simultaneously lowers ram pressure and ram drag, which causes a beneficial reduction in TSFC and a decrease in propulsive efficiency of the turbofan engine. These opposing trends of TSFC and propulsive efficiency with respect to flight speed are also documented by Torenbeek [33, Ch. 4].

The temperature response over the next 100 years is presented in Figure 12 for the three objectives. The difference in the climate impact of the three aircraft becomes apparent in this figure since the ATR_{100} objective is related to the area under these curves. The line corresponding to the fuel mass objective shows a relatively high maximum in 2075 because the short-term climate effects are prevailing, while the impact of long-lived CO_2 emissions (which relate linearly to fuel consumption) is reduced. For the climate-optimized case, the short-term effects are minimized, but the maximum occurs later due to the delayed effect of CO_2 emissions.

Additionally, upon further examination of Figure 12, the surface temperature change in the year 2120 approaches approximately 20-25 mK for all cases. Hence, one may argue that the final effect is the same. Nevertheless, the climate-optimized airplane does not reach the same level of temperature change around 2075. This is captured by the ATR_{100} metric and shows that this metric can give insight into global warming by capturing short- and long-term effects of several species.

A final remark on the fixed productivity approach is that approximately 13% more aircraft have to be produced in case of the climate-optimized aircraft, at a higher production rate, to reach the same productivity level in the period from 2050 to 2055. This is indicated in Figure 10. The need for more aircraft is a consequence of the higher block time, which reduces the productivity of a single aircraft. To maintain the same level of fleet productivity, more aircraft of this type have to operated. Nor the climate impact, nor the costs of this larger production capacity are computed in this research. However, one could argue qualitatively that this increased production raises both the climate footprint and the complete lifecycle cost of the climate-optimized aircraft.

During the operational lifetime of this aircraft, from 2020 to 2085, the technology levels will likely evolve and affect the propulsion, aerodynamic and structural disciplines. This study does not quantify the impact of such developments on the optimized aircraft. Nevertheless, a qualitative outlook is provided here. Since a single aircraft type is considered with a market introduction in 2020, the airframe will remain almost constant throughout the considered lifespan, albeit with minor aerodynamic and structural improvements. These improvements can enhance the cruise efficiency, leading to lower fuel burn and reduced absolute emissions. Although the aircraft mass alters contrail properties [56], the effect is mainly dependent on aircraft category and is difficult to quantify in the conceptual phase. An engine upgrade during
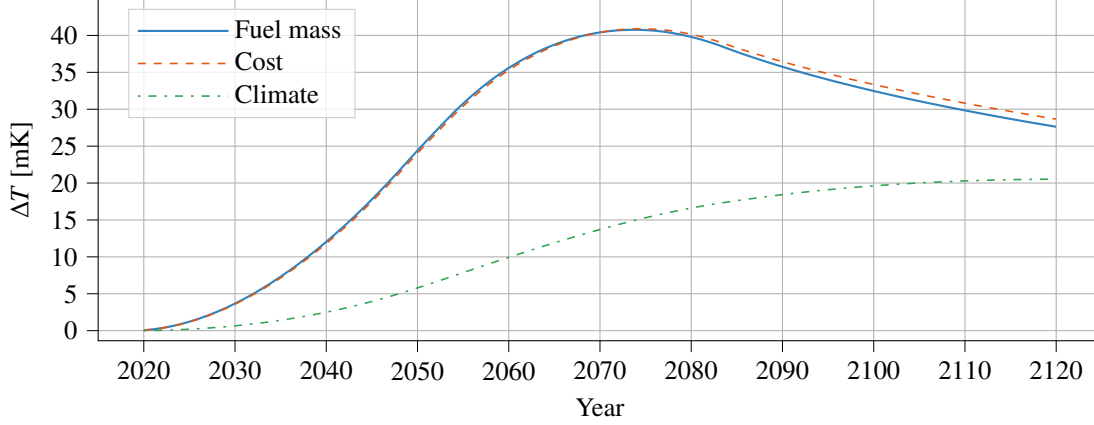
Fig. 12 Surface temperature change for the three objective functions

Table 11 Performance indicators of optimized aircraft

Parameter	Fuel Mass	COC	ATR$_{100}$
MTOM [metric tons]	68.5	68.2	66.9
OEM [metric tons]	38.5	37.4	36.0
S [m^2]	111	121	108
$\Lambda_{0.25}$ [deg]	16.3	22.0	0.0
λ [-]	0.325	0.277	0.460
$(L/D)_{\mathrm{cr}}$ [-]	19.3	18.2	18.8
$(T/W)_{\mathrm{TO}}$ [-]	0.329	0.315	0.317
T_{TO} [kN]	221	211	207
TSFC$_{\mathrm{cr}}$ [kg/(N s)]	1.51	1.61	1.47
t_{bl} [hrs]	3.62	3.49	3.95
$N_{\mathrm{AC,\,max}}$ [-]	15226	14663	16637

the aircraft's lifetime is feasible, which can drastically influence the overall fuel burn and emissions through improved component efficiencies and combustor design. Producing less NO$_\mathrm{x}$ emissions at higher overall pressure ratios would be beneficial, and could increase the optimal cruise altitude and Mach number. A study with updated design assumptions, such as increased aspect ratio, bypass ratio and temperature bounds, is recommended to reflect on future technology levels, considering a later entry into the market. Next to the aerodynamic and possible efficiency benefits, also the effect of such technologies on other disciplines such as mass should be properly taken into account in the methods.

C. Multi-Objective Optimization Results

This section describes the results of multi-objective optimization to study the trade-off between climate impact and operating costs. The Pareto front defining this trade-off is presented in Figure 13. This image shows that for a marginal cash-operating cost increase of 1 to 2%, already a significant reduction in ATR$_{100}$ is possible. This large reduction

potential comes mostly from the reduction in cruise altitude and Mach number. Although uncertainties remain, it seems that to significantly lower the climate impact while limiting the cost increase, a design solution near a 50% ATR_{100} reduction and 2% cost increase is preferred over the climate-optimal solution. Beyond this point, the costs rise more rapidly for a marginal decrease in climate impact.
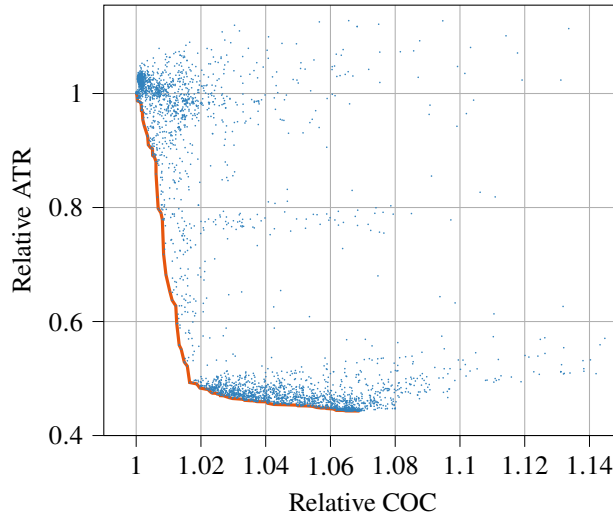

Fig. 13 Pareto front (orange line) between cost and climate objectives (the data is normalized with respect to the cost-optimal aircraft, blue dots are feasible designs)

D. Comparison with Literature

To put these results in perspective and highlight key findings, we compare the optimized designs with previous research by Dallara and Kroo [7] and Koch [13]. In essence, it can be concluded that the main design trends for climate-optimal aircraft are similar: lower cruise altitude at reduced Mach number, combined with a higher aspect ratio and bypass ratio, compared to cost-optimal aircraft. Dallara and Kroo report a reduction in ATR_{100} of 35 to 74% depending on the discount rate (0 or 3%, respectively). In this study the climate reduction is estimated to be approximately 57%, assuming a discount rate of zero.

We expect that the main reason for this discrepancy in climate impact reduction is the difference in the contrail effects. The cost-optimal solution in this research has a relative contrail contribution of approximately 48%, while in the case of Dallara and Kroo this contribution is only 17%. Hence, the achievable relative reduction becomes larger when the contrails vanish due to the lower cruise flight. The cost increase for the climate-optimal aircraft appears to be similar for both studies, as can be concluded from the Pareto fronts. This cost rise is approximately 6 to 10%. Small discrepancies may be the result of a different definition of the costs and distinct price assumptions. Especially the ratio between fuel costs and time-related costs, such as salaries, performs an important role in this analysis.

Although the two studies are comparable, the current research also offers insight into the optimal engine parameters.

For example, the trend in OPR shows that climate-optimal aircraft do not feature a maximum OPR, presumably to lower the emission index of nitrogen oxides. The engine efficiency of the climate-optimal is also lower than for the fuel-optimal aircraft. This engine efficiency also performs a role in the contrail formation. Furthermore, due to span constraints, the aspect ratio cannot achieve values of nineteen or twenty, as is the case for the optimization by Dallara and Kroo. This further limits the cruise efficiency of the climate-optimal aircraft and leads to a higher fuel burn. Nevertheless, considering current airport constraints and technology levels, this span constraint possibly makes the design more realistic.

V. Conclusions and Recommendations

This paper aims to research the relationship between designing for minimal climate impact and minimal operating costs. To this end, a multidisciplinary and multi-objective optimization framework is arranged to study the influence of wing, turbofan and mission design variables on global warming impact, measured by the average temperature response, and direct operating costs, expressed in USD. For a fixed fleet productivity level, it is estimated that the ATR_{100} can be reduced by approximately 57% when moving from the cost objective to the climate objective, at the expense of an 6.9% increase in operating costs. Although these values are based on a simplified analysis and are subject to uncertainties, it indicates that these objectives are indeed conflicting. The reduction in ATR_{100} can be achieved by lowering the cruise altitude to 7.6 km, flying at Mach 0.60 and by decreasing the engine overall pressure ratio compared to the fuel-optimized case, from 57 to approximately 37. These changes are driven by non-CO_2 effects, namely the emission of nitrogen oxides and the formation of contrails.

Flying slower causes the block time of the climate-optimized aircraft to be higher than for the aircraft designed for fuel-burn or cost, which reduces its productivity compared to these alternatives. For a hypothetical fleet with constrained productivity, it is concluded that approximately 13% more climate-optimized aircraft are needed than cost-optimized aircraft, to achieve the same level of productivity on a fleet level.

Finally, four recommendations for further research can be formulated. Firstly, the operational scenario can be made more realistic by assessing the aircraft performance and emissions for varying load factors and stage lengths. Operators deploy aircraft more flexibly, unlike the fixed mission in the current research. Secondly, it would be of interest to carry out this optimization for other aircraft categories, possibly with propeller technologies. Additionally, a simultaneous optimization of the aircraft design and mission trajectory is recommended to examine whether the climate impact can be reduced further. Finally, it has to be noted that the current framework employs a simplified climate model. Climate functions for aircraft design derived from more advanced models, as proposed in the GLOWOPT project, can offer a more accurate evaluation.

Appendix

A. Input Data for Propulsion Discipline Verification and Validation

The conditions and data presented in Tables 12 and 13 are adopted to model the General Electric GE90 engine for verification and validation purposes in Section III.A.

Table 12   Design requirements assumed for the GE90 engine model

Operating Condition	Net Thrust [kN]	Altitude [km]	Mach [-]	ΔT_{ISA} [K]
Cruise	77.85	10.67	0.80	0.00
Take-off	376.80	0.00	0.00	15.00

Table 13   Design parameters assumed in the model of the GE90 engine at design point (cruise) [35, 57, 58]

Component	Parameter	Value	Unit
Inlet	Total pressure loss ΔP_T	0.980	-
Fan	Bypass Ratio BPR	8.50	-
	Total pressure ratio Π_{fan}	1.58	-
	Polytropic efficiency η_{pol}	0.915	-
Low Pressure Compressor	Total pressure ratio Π_{lpc}	1.26	-
	Polytropic efficiency η_{pol}	0.910	-
High Pressure Compressor	Total pressure ratio Π_{hpc}	20.0	-
	Polytropic efficiency η_{pol}	0.900	-
Combustor	Total pressure loss ΔP_T	0.950	-
	Combustion efficiency η_{comb}	0.990	-
	Turbine entry temperature TET	1430	K
High Pressure Turbine	Polytropic efficiency η_{pol}	0.930	-
	Mechanical efficiency η_{mech}	0.990	-
Low Pressure Turbine	Polytropic efficiency η_{pol}	0.930	-
	Mechanical efficiency η_{mech}	0.990	-

B. Input Data for Aircraft Synthesis Verification

Table 14 presents the top-level airplane requirements for the Airbus A320-200 and Boeing 777-200 aircraft employed for verification and validation in Section III.B.

Table 14   Top-level airplane requirements employed for the aircraft synthesis verification and validation [50]

Requirement [Unit]	Airbus A320-200	Boeing 777-200
Maximum structural payload [metric tons]	18.2	54.9
Harmonic range [10^3 km (10^3 nm)]	3200 (1730)	6000 (3200)
Cruise Mach number [-]	0.78	0.84
Cruise altitude [km (FL)]	11.3 (37)	11.9 (39)
Approach speed [m/s (kts)]	70.0 (136)	70.0 (136)
Take-off length (ISA conditions) [m (ft)]	2200 (7220)	2440 (8010)

C. Geometry Creation Methodology

Based on the design variables, a separate module creates a conceptual geometry of the aircraft employing empirical, statistical and physics-based relations. Data from the geometry model propagates to the aerodynamic and Class-II mass estimation disciplines to compute the zero-lift drag component and structural mass, respectively. This section summarizes the methods used to create the conceptual outer line of the aircraft.

1. Fuselage

Since the passenger number and mission range are the main drivers for the fuselage, the geometry remains the same throughout the optimization iterations. This is because the inputs for the fuselage, namely the TLARs and design assumptions per aircraft category, are held constant. The fuselage geometry methodology consists of three steps. Firstly, the cabin cross-section is designed. The number of seats abreast is determined from the maximum number of passengers ($N_{\text{pax, max}}$), in an all-economy layout, according to the following relation:

$$N_{\text{seats abreast}} = \max \left(\left\lfloor 0.47 \cdot \sqrt{N_{\text{pax, max}}} \right\rfloor, 6 \right) \tag{30}$$

One aisle is introduced if the number of seats abreast is 6 or lower, while two aisles are considered for more seats. The required cabin width is then determined from a summation of seat and aisle widths, assuming the parameters in Table 15 which are derived from existing cabin layouts [51, 52, 59, 60]. Based on the cabin width and the unit load device (ULD) selection, the smallest possible inner cross-section radius is determined. To determine the outer diameter of the cross-section (d_{outer}), constant thicknesses are assumed according to the values in Table 15.

Secondly, the longitudinal layout of the fuselage is created. The interior of the fuselage consists of three parts: the cockpit, cabin and tail. The total length of the fuselage is the sum of the lengths of these three sections. The number of

Table 15 Assumed parameters and design choices to determine the fuselage geometry

	Narrow-body ($\leq$ 6 seats abreast)	Wide-body (> 6 seats abreast)
Seat width [m (inch)]	0.457 (18.0)	0.457 (18.0)
Aisle width [m (inch)]	0.457 (18.0)	0.584 (23.0)
Armrest width [m (inch)]	0.05 (1.97)	0.05 (1.97)
Cabin length factor k_{cabin} [-]	0.900	1.17
Cross-section d_{outer} [m (inch)]	d_{inner} + 0.150 (5.91)	d_{inner} + 0.340 (13.4)
Loading device	LD3-45	2 x LD2 or LD3

rows multiplied by a statistical factor, k_{cabin}, determines the cabin length according to

$$N_{rows} = \frac{N_{pax,\,max}}{N_{seats\ abreast}} \tag{31}$$

$$l_{cabin} = k_{cabin} \cdot N_{rows} \tag{32}$$

The factor k_{cabin} also accounts for the length due to galley areas and exits. The total fuselage length follows by adding the cockpit length (assumed to be 4 m) and the tail length, which is assumed to be 1.6 times the outer cabin diameter.

Finally, the outer geometry of the fuselage is shaped. Similar to the inner layout, three distinct sections are considered: the nosecone, central fuselage and tailcone. The nose- and tailcones are longer than their respective interior sections, while the center fuselage is shorter than the cabin. For the nosecone, a finess ratio of 1.3 with respect to d_{outer} is assumed, while for the tailcone this ratio is 3. Subsequently, the length of the central part is equal to the total length of the fuselage, minus the lengths of the nose- and tailcone sections.

The central section of the fuselage is assumed to be a cylinder with a diameter equal to d_{outer}. The nosecone cross-sectional area decreases parabolically towards the nose point, which is located slightly below the fuselage center line according to a 4-degree droop angle measured from the front section of the central part. The tailcone starts tangentially to the central fuselage section and grows smoothly towards the tail point which is located above the fuselage central line, taking into account an upsweep of 7 degrees.

2. Wing Planform

The design vector contains two variables that directly influence the wing geometry, namely the aspect ratio and the wing loading. The wing surface area S follows from dividing (MTOM $\cdot$ g) by the wing loading. This area includes a trapezoidal section covered by the fuselage. The total wing span b then results from the surface area and the aspect ratio. The area S and span b establish the main dimensions, but do not fully define the wing planform. The other parameters required to conceptually determine the drag coefficient and structural mass are the quarter-chord sweep angle, taper ratio, and root and tip chord thicknesses.

In this study, it is assumed that the quarter-chord sweep angle ($\Lambda_{0.25}$) is driven by the cruise Mach number according to the following statistical relationship for transport aircraft, based on data from References [33] and [61]:

$$\Lambda_{0.25} = \begin{cases} 0 & \text{if } M_{\text{cr}} < 0.66 \\ \arccos\left(\frac{1.16}{M_{\text{cr}}+0.5}\right) & \text{if } M_{\text{cr}} \geq 0.66 \end{cases} \tag{33}$$

The taper ratio of the wing has to be adjusted according to the sweep angle to unload the tip section at higher sweep angles. Conceptually, the taper ratio can be related to the quarter-chord sweep angle as follows:

$$\lambda = -0.0083 \cdot \Lambda_{0.25} + 0.4597 \tag{34}$$

Furthermore, the trailing edge sweep angle is zero up to 30% of the semi-span to facilitate easier integration of the landing gear and high-lift devices, which are placed perpendicular to the freestream flow direction. This assumption, combined with the above parameters, fully defines the top-view planform of the wing.

Although the exact 3D outer mold line of the wing is not created, the aerodynamic and structural modules require an approximation of the root- and tip-chord thicknesses. The following relations provide such estimates [62]:

$$t/c_{\text{tip}} = \max\left(\min\left[\frac{\cos^3\left(\Lambda_{0.5}\right) \cdot [0.935 - (M_{\text{cr}} + 0.03) \cdot \cos\left(\Lambda_{0.5}\right)] - 0.115 \cdot C_{L,\text{cr}}^{1.5}}{\cos^2\left(\Lambda_{0.5}\right)}, 0.18\right], 0.10\right) \tag{35}$$

$$t/c_{\text{root}} = t/c_{\text{tip}} + 0.03 \tag{36}$$

The twist and dihedral angles are not considered in the current approach, since the implemented methods are not sensitive to these parameters. The longitudinal position of the wing is determined simultaneously with the empennage size. Therefore, this aspect is discussed in the subsequent section.

3. Empennage Planform and Wing Placement

The geometry module employs tail volume coefficients to determine the areas of the horizontal and vertical tail surfaces. The volume coefficients are derived from statistical data and are assumed to be independent of the design choices made by the optimizer. The respective surface areas, S_{ht} and S_{vt}, follow from the definitions of the volume coefficients for the horizontal ($\overline{V}_{\text{ht}}$) and vertical $\overline{V}_{\text{vt}}$ tail.

$$\overline{V}_{\text{ht}} = \frac{\left(x_{\text{ht}} - x_{\text{cg, aft}}\right) S_{\text{ht}}}{S \cdot \text{MAC}} \Rightarrow S_{\text{ht}} = \overline{V}_{\text{ht}} \cdot \frac{S \cdot \text{MAC}}{x_{\text{ht}} - x_{\text{cg, aft}}} \tag{37}$$

$$\overline{V}_{\text{vt}} = \frac{\left(x_{\text{vt}} - x_{\text{cg, aft}}\right) S_{\text{vt}}}{S \cdot b} \Rightarrow S_{\text{vt}} = \overline{V}_{\text{vt}} \cdot \frac{S \cdot b}{x_{\text{vt}} - x_{\text{cg, aft}}} \tag{38}$$

In the above equations, x_{ht} and x_{vt} represent the longitudinal position of the aerodynamic center of the horizontal and vertical tails, respectively, while $x_{cg, aft}$ is the x-coordinate of the most aft center-of-gravity position. The former two are set at 91% and 92% of the fuselage length, respectively. The statistical values for the tail volume coefficients are included in Table 16.

The operational cg excursion determines $x_{cg, aft}$ based on the position of the OEM cg location $x_{cg, OEM}$, and the varying locations of payload and fuel. However, to obtain $x_{cg, OEM}$, first the longitudinal position of the wing has to be fixed. The latter position, defined by the leading edge of the MAC ($x_{LE, MAC}$), can be calculated from the masses of the main structural groups and their relative locations, as well the assumed position of the OEM cg location with respect to the mean aerodynamic chord, $\xi_{cg, OEM} = 0.25$. ξ is the longitudinal coordinate with respect to the mean aerodynamic chord ($\xi = (x - x_{LE, MAC}) / \bar{c}$). The wing position $x_{LE, MAC}$, measured from the fuselage nose point, is computed as follows:

$$x_{LE, MAC} = x_{cg, FG} + \bar{c} \cdot \left[\xi_{cg, WG} \cdot \frac{m_{WG}}{m_{FG}} - \xi_{cg, OEM} \cdot \left(1 + \frac{m_{WG}}{m_{FG}} \right) \right]$$

$$\text{where } x_{cg, FG} = \frac{x_{fus} m_{fus} + x_{ht} m_{ht} + x_{vt} m_{vt} + x_{fe} m_{fe}}{m_{fus} + m_{ht} + m_{vt} + m_{fe}}, \text{ and } \xi_{cg, WG} = \frac{\xi_w m_w + \xi_{eng} m_{eng}}{m_w + m_{eng}}$$

(39)

The parameter $\bar{c}$ is the absolute length of the mean aerodynamic chord in the above equations. The masses of the groups, being the wing (w), fuselage (fus), engines (eng), empennage (ht and vt) and fixed equipment (fe), result directly from the Class-II mass estimation (Section II.B.3). The positions of the fuselage, empennage and fixed equipment (fuselage group, FG) are expressed relative to the fuselage length, while the locations of the wing and engine masses (wing group, WG) are anchored to the MAC. The value of $x_{LE, MAC}$ allows to compute $x_{cg, OEM}$ and $x_{cg, aft}$, leading to the tail arms in Equations (37) and (38). The assumed relative positions in Equation (39) are gathered in Table 16. The relative position of the engines with respect to the MAC (ξ_{eng}) has to be determined for the design under consideration since it is dependent on the wing and engine parameters.

Table 16   Assumed parameters and design choices to determine the empennage geometry

	Narrow-body	Wide-body
$\overline{V}_{ht}$	1.1	0.70
$\overline{V}_{vt}$	0.085	0.060
x_{fus}/l_{fus}	0.45	
x_{ht}/l_{fus}	0.91	
x_{vt}/l_{fus}	0.92	
x_{fe}/l_{fus}	0.45	
ξ_w	0.40	

4. Nacelles

The nacelles around the turbofan engines have a cylindrical shape in the current model. Although this is a simplification, it provides the necessary data to estimate the drag contribution. The diameter of the nacelles is based on the fan diameter, which is estimated from the mass flow entering the engine according to the following relation:

$$d_{\text{nac}} = 1.15 \cdot d_{\text{fan}} = 1.15 \cdot 2 \cdot \sqrt{\frac{A_{\text{fan}}}{\pi \cdot \left(1 - ht_{\text{fan}}^2\right)}} \quad \text{with} \quad A_{\text{fan}} = \dot{m}_{0,\text{TOC}} \cdot \frac{\sqrt{T_{t2}}}{p_{t2} \cdot \text{mfp}_2} \tag{40}$$

In the above equation, ht_{fan} is the fan hub-to-tip ratio (0.33), $\dot{m}_{0,\text{TOC}}$ is the total mass flow at top-of-climb conditions, T_{t2}, p_{t2}, and mfp_2 the total temperature, total pressure and mass flow parameter [29] at the fan inlet face. The latter is calculated from the total temperature at this station and an axial Mach number of 0.6 [30]. The length of the nacelle, in meter, is computed from the following statistical relation provided by Torenbeek and Berenschot [63]:

$$l_{\text{nac}} = 7.8 \left(\sqrt{\frac{\dot{m}_{0,\text{TO}}}{\rho_0 \cdot a_0} \cdot \frac{1 + 0.2 \cdot \text{BPR}_{\text{TO}}}{1 + \text{BPR}_{\text{TO}}}} + 0.10 \right) \tag{41}$$

VI. Optimization Setup and Convergence

This appendix briefly discusses the optimization strategy employed to obtain the results in Section IV. The following three consecutive steps are carried out for the single-objective optimizations:

1) The design space is explored through design of experiments (DOE), using Latin Hypercube Sampling (LHS).

2) Global search algorithms are applied to the find design subspace which minimizes the objective under consideration. This helps with discrete steps in the design space, such as the formation condition of contrails. A genetic algorithm, or derived method, is used in this case.

3) The final step is to refine the optimal solution and ensure the solver converges. To achieve this, the Nelder-Mead algorithm is employed with a termination accuracy of 1.0×10^{-4} on the objective value. Although gradient-based methods, such as SQP, also proved to be suitable for this step, the Nelder-Mead method appeared to be more robust.

The convergence in the final step is illustrated in Figure 14 for the fuel mass objective. Note that in this case, the optimizer decided the initial point with which the objective function and design variable values are normalized. Furthermore, the constraints are formulated such that the value of g has to be non-negative. To obtain the Pareto front in Section IV.C a multi-strategy algorithm named pilOPT is employed which is available in modeFRONTIER [‡] software. This multi-objective algorithm automatically selects the best approach based on the problem formulation and DOE data, and continues until not enough strictly dominating designs are found anymore.

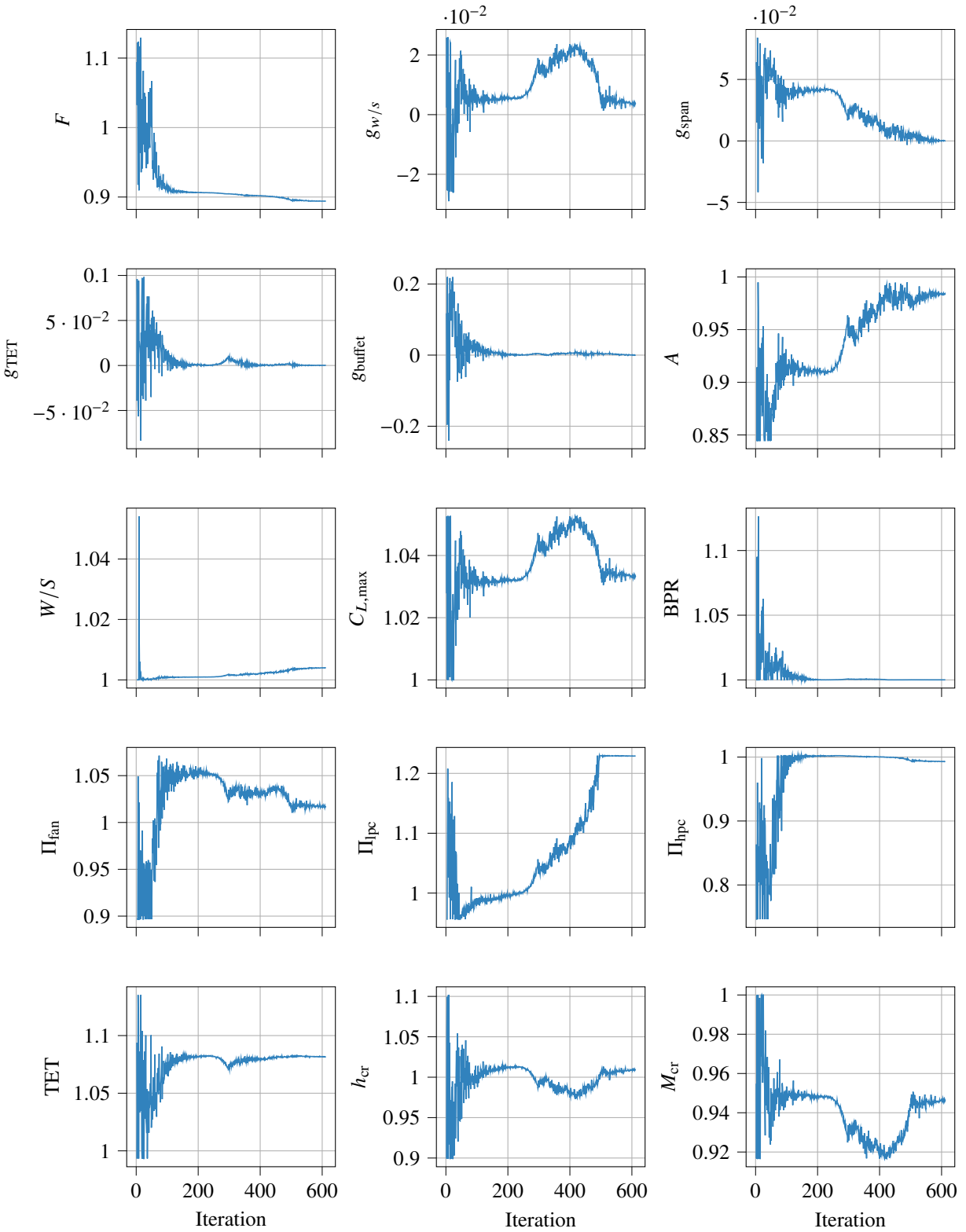[‡]URL `https://engineering.esteco.com/modefrontier` accessed on 16/02/2022

Fig. 14 Convergence plots of objective function, constraints, and design variables for fuel mass minimization

Funding Sources

Acknowledgments

References

[1] Lee, D., Pitari, G., Grewe, V., Gierens, K., Penner, J., Petzold, A., Prather, M., Schumann, U., Bais, A., Berntsen, T., Iachetti, D., Lim, L., and Sausen, R., "Transport impacts on atmosphere and climate: Aviation," *Atmospheric Environment*, Vol. 44, No. 37, 2010, pp. 4678–4734. https://doi.org/10.1016/j.atmosenv.2009.06.005.

[2] Lee, D. S., Fahey, D. W., Skowron, A., Allen, M. R., Burkhardt, U., Chen, Q., Doherty, S. J., Freeman, S., Forster, P. M., Fuglestvedt, J., Gettelman, A., De León, R. R., Lim, L. L., Lund, M. T., Millar, R. J., Owen, B., Penner, J. E., Pitari, G., Prather, M. J., Sausen, R., and Wilcox, L. J., "The contribution of global aviation to anthropogenic climate forcing for 2000 to 2018," *Atmospheric Environment*, Vol. 244, 2021, p. 117834. https://doi.org/10.1016/j.atmosenv.2020.117834.

[3] Airbus, *Global Market Forecast - Cities, Airports and Aircraft 2019-2038*, 5th ed., Airbus S.A.S., Blagnac Cedex, 2019.

[4] Boeing, *Commercial Market Outlook 2019-2038*, Boeing, 2019.

[5] Antoine, N. E., and Kroo, I. M., "Framework for Aircraft Conceptual Design and Environmental Performance Studies," *AIAA Journal*, Vol. 43, No. 10, 2005, pp. 2100–2109. https://doi.org/10.2514/1.13017.

[6] Dahlmann, K., Koch, A., Linke, F., Lührs, B., Volker, G., Otten, T., Seider, D., Gollnick, V., and Schumann, U., "Climate-Compatible Air Transport System—Climate Impact Mitigation Potential for Actual and Future Aircraft," *Aerospace*, Vol. 3, 2016, p. 38. https://doi.org/10.3390/aerospace3040038.

[7] Dallara, E. S., and Kroo, I., "Aircraft Design for Reduced Climate Impact," *49th AIAA Aerospace Sciences Meeting including the New Horizons Forum and Aerospace Exposition*, American Institute of Aeronautics and Astronautics, Orlando, Florida, 2011. https://doi.org/10.2514/6.2011-265.

[8] Grewe, V., Dahlmann, K., Flink, J., Frömming, C., Ghosh, R., Gierens, K., Heller, R., Hendricks, J., Jöckel, P., Kaufmann, S., Kölker, K., Linke, F., Luchkova, T., Lührs, B., Van Manen, J., Matthes, S., Minikin, A., Niklaß, M., Plohr, M., Righi, M., Rosanka, S., Schmitt, A., Schumann, U., Terekhov, I., Unterstrasser, S., Vázquez-Navarro, M., Voigt, C., Wicke, K., Yamashita, H., Zahn, A., and Ziereis, H., "Mitigating the Climate Impact from Aviation: Achievements and Results of the DLR WeCare Project," *Aerospace*, Vol. 4, No. 3, 2017, p. 34. https://doi.org/10.3390/aerospace4030034.

[9] Henderson, R. P., Martins, J. R. R. A., and Perez, R. E., "Aircraft conceptual design for optimal environmental performance," *The Aeronautical Journal (1968)*, Vol. 116, No. 1175, 2012, p. 1–22. https://doi.org/10.1017/S000192400000659X.

[10] Chai, X., Yu, X., and Wang, Y., "Tradeoff Study between Cost and Environmental Impact of Aircraft Using Simultaneous Optimization of Airframe and Engine Cycle," *International Journal of Aerospace Engineering*, Vol. 2017, 2017, pp. 1–10. https://doi.org/10.1155/2017/2468535.

[11] Egelhofer, R., Bickerstaff, C., and Bonnet, S., "Minimizing Impact on Climate in Aircraft Design," *SAE Technical Paper*, SAE International, 2007. https://doi.org/10.4271/2007-01-3807.

[12] Wang, Y., Xing, Y., Yu, X., and Zhang, S., "Flight operation and airframe design for tradeoff between cost and environmental impact," *Proceedings of the Institution of Mechanical Engineers, Part G: Journal of Aerospace Engineering*, Vol. 232, No. 5, 2018, pp. 973–987. https://doi.org/10.1177/0954410017748967.

[13] Koch, A., "Climate Impact Mitigation Potential given by Flight Profile and Aircraft Optimization," Phd, Technischen Universität Hamburg-Harburg, Hamburg, Germany, Nov 2013. https://doi.org/10.13140/RG.2.1.4896.9047.

[14] Grewe, V., and Stenke, A., "AirClim: an efficient tool for climate evaluation of aircraft technology," *Atmospheric Chemistry and Physics*, Vol. 8, No. 16, 2008, pp. 4621–4639. https://doi.org/10.5194/acp-8-4621-2008.

[15] Schutte, J., and Mavris, D. N., "Evaluation of N+2 Technologies and Advanced Vehicle Concepts," *53rd AIAA Aerospace Sciences Meeting*, Kissimmee, Florida, 2015. https://doi.org/10.2514/6.2015-0514.

[16] Design Science and Technology Sub Group, "Air Travel – Greener by Design Mitigating the environmental impact of aviation: Opportunities and priorities," *The Aeronautical Journal (1968)*, Vol. 109, No. 1099, 2005, p. 361–416. https://doi.org/10.1017/S0001924000000841.

[17] Herbon, J., Aicholtz, J., Hsieh, S.-Y., Viars, P., Birmaher, S., Brown, D., Patel, N., Carper, D., Cooper, C., and Fitzgerald, R., "N+2 Advanced Low NOx Combustor Technology Final Report," Tech. Rep. NASA/CR-2017-219410, National Aeronautics and Space Administration (NASA), 2017.

[18] Schumann, U., "Influence of propulsion efficiency on contrail formation," *Aerospace Science and Technology*, Vol. 4, No. 6, 2000, pp. 391–401. https://doi.org/10.1016/S1270-9638(00)01062-2.

[19] Reynolds, T., Barrett, S., Dray, L., Evans, A., Köhler, M., Vera-Morales, M., Schäfer, A., Wadud, Z., Britter, R., Hallam, H., and Hunsley, R., "Modelling Environmental and Economic Impacts of Aviation: Introducing the Aviation Integrated Modelling Project," *7th AIAA ATIO Conf, 2nd CEIAT Int'l Conf on Innov and Integr in Aero Sciences,17th LTA Systems Tech Conf; followed by 2nd TEOS Forum*, Belfast, Northern Ireland, 2007. https://doi.org/10.2514/6.2007-7751.

[20] Bernardo, J. E., Zaidi, T., LeVine, M., Jimenez, H., and Mavris, D., "Rapid Integrated Interdependent Fleet-Level Environmental Model," *Journal of Aircraft*, Vol. 54, No. 3, 2017, pp. 939–954. https://doi.org/10.2514/1.C033572.

[21] LeVine, M. J., Bernardo, J. E., Kirby, M., and Mavris, D. N., "Average Generic Vehicle Method for Fleet-Level Analysis of Noise and Emission Tradeoffs," *Journal of Aircraft*, Vol. 55, No. 3, 2018, pp. 929–946. https://doi.org/10.2514/1.C034368.

[22] Vera-Morales, M., and Hall, C. A., "Modeling Performance and Emissions from Aircraft in the Aviation Integrated Modelling Project," *Journal of Aircraft*, Vol. 47, No. 3, 2010, pp. 812–819. https://doi.org/10.2514/1.44020.

[23] Moolchandani, K., Govindaraju, P., Roy, S., Crossley, W. A., and DeLaurentis, D. A., "Assessing Effects of Aircraft and Fuel Technology Advancement on Select Aviation Environmental Impacts," *Journal of Aircraft*, Vol. 54, No. 3, 2017, pp. 857–869. https://doi.org/10.2514/1.C033861.

[24] Jimenez, H., Pfaender, H., and Mavris, D., "Fuel Burn and CO2 System-Wide Assessment of Environmentally Responsible Aviation Technologies," *Journal of Aircraft*, Vol. 49, No. 6, 2012, pp. 1913–1930. https://doi.org/10.2514/1.C031755.

[25] McEnteggart, Q., and Whidborne, J. F., "Multiobjective Environmental Departure Procedure Optimization," *Journal of Aircraft*, Vol. 55, No. 3, 2018, pp. 905–917. https://doi.org/10.2514/1.C033132.

[26] Mori, R., "Fuel-Saving Climb Procedure by Reduced Thrust near Top of Climb," *Journal of Aircraft*, Vol. 57, No. 5, 2020, pp. 800–806. https://doi.org/10.2514/1.C035200.

[27] Lührs, B., Niklass, M., Froemming, C., Grewe, V., and Gollnick, V., "Cost-Benefit Assessment of 2D and 3D Climate And Weather Optimized Trajectories," *16th AIAA Aviation Technology, Integration, and Operations Conference*, Washington, D.C., 2016. https://doi.org/10.2514/6.2016-3758.

[28] Hwang, J. T., Jasa, J. P., and Martins, J. R. R. A., "High-Fidelity Design-Allocation Optimization of a Commercial Aircraft Maximizing Airline Profit," *Journal of Aircraft*, Vol. 56, No. 3, 2019, pp. 1164–1178. https://doi.org/10.2514/1.C035082.

[29] Mattingly, J. D., Heiser, W. H., and Pratt, D. T., *Aircraft Engine Design, Second Edition*, American Institute of Aeronautics and Astronautics (AIAA), Reston, Virginia, 2002. https://doi.org/10.2514/4.861444.

[30] Obert, E., *Aerodynamic Design of Transport Aircraft*, IOS press, 2009.

[31] Lambe, A. B., and Martins, J. R., "Extensions to the Design Structure Matrix for the Description of Multidisciplinary Design, Analysis, and Optimization Processes," *Structural and Multidisciplinary Optimization*, Vol. 46, No. 2, 2012, p. 273–284. https://doi.org/10.1007/s00158-012-0763-y.

[32] Roskam, J., *Airplane Design. Part I: Preliminary Sizing of Airplanes*, DARcorporation, 1985.

[33] Torenbeek, E., *Synthesis of Subsonic Airplane Design*, Delft University Press and Kluwer Academic Publishers, Dordrecht, 1982.

[34] Walsh, P. P., and Fletcher, P., *Gas turbine performance*, 2nd ed., Blackwell Science Ltd, Oxford, 2004. https://doi.org/10.1002/9780470774533.

[35] Greitzer, E. M., Bonnefoy, P., de la Rosa Blanco, E., Dorbian, C., Drela, M., Hall, D., Hansman, R., Hileman, J., Liebeck, R., Lovegren, J., Mody, P., Pertuze, J., Sato, S., Spakovszky, Z., Tan, C., Hollman, J., Duda, J., Fitzgerald, N., Houghton, J., Kerrebrock, J., Kiwada, G., Kordonowy, D., Parrish, J., Tylko, J., Wen, E., and Lord, W., "N+3 Aircraft Concept Designs and Trade Studies. Volume 2: Appendices - Design Methodologies for Aerodynamics, Structures, Weight, and Thermodynamic Cycles," Tech. Rep. NASA/CR-2010-216794/VOL2, National Aeronautics and Space Administration (NASA), 2010.

[36] Torenbeek, E., "The initial calculation of range and mission fuel during conceptual design," Tech. Rep. LR-525, Delft University of Technology, Faculty of Aerospace Engineering, 1987.

[37] Grewe, V., and Dahlmann, K., "How ambiguous are climate metrics? And are we prepared to assess and compare the climate impact of new air traffic technologies?" *Atmospheric Environment*, Vol. 106, 2015, pp. 373–374. https://doi.org/10.1016/j.atmosenv.2015.02.039.

[38] Sausen, R., and Schumann, U., "Estimates of the Climate Response to Aircraft CO_2 and NO_x Emissions Scenarios," *Climate Change*, Vol. 44, 2000, pp. 27 – 58. https://doi.org/10.1023/A:1005579306109.

[39] IPCC, *Climate Change 2007 - The physical science basis. Working group I. Contributions to the Fourth Assessment Report of the Intergovernmental Panel of Climate Change*, Cambridge University Press, New York, NY, USA, 2007.

[40] Ponater, M., Pechtl, S., Sausen, R., Schumann, U., and Hüttig, G., "Potential of the cryoplane technology to reduce aircraft climate impact: A state-of-the-art assessment," *Atmospheric Environment*, Vol. 40, No. 36, 2006, pp. 6928–6944. https://doi.org/10.1016/j.atmosenv.2006.06.036.

[41] Schwartz Dallara, E., Kroo, I. M., and Waitz, I. A., "Metric for Comparing Lifetime Average Climate Impact of Aircraft," *AIAA Journal*, Vol. 49, No. 8, 2011, pp. 1600–1613. https://doi.org/10.2514/1.J050763.

[42] Fahey, D. W., Baughcum, S. L., Gupta, M., Lee, D. S., Sausen, R., and van Velthoven, P., "Aviation and Climate: State of Science," Tech. rep., ICAO, 2013.

[43] Schwartz Dallara, E., "Aircraft Design for Reduced Climate Impact," Phd, Stanford University, Stanford, CA, USA, Feb 2011.

[44] Grewe, V., Matthes, S., and Dahlmann, K., "The contribution of aviation NO_x emissions to climate change: are we ignoring methodological flaws?" *Environmental Research Letters*, Vol. 14, No. 12, 2019, p. 121003. https://doi.org/10.1088/1748-9326/ab5dd7.

[45] Sonntag, D., "Important new values of the physical constants of 1986, vapour pressure formulations based on the ITS-90, and psychrometer formulae," *Zeitschrift für Meteorologie*, Vol. 40, No. 5, 1990, pp. 340–344.

[46] Roskam, J., *Airplane Design. Part VIII: Airplane Cost Estimation: Design, Development, Manufacturing and Operating*, DARcorporation, 1985.

[47] Airbus Media Relations, "2018 price adjustment across Airbus' modern product range reflects continuous investment and customer value," , 2018. URL https://www.airbus.com/content/dam/corporate-topics/publications/press-release/new-airbus-list-prices-2018.pdf.

[48] The Boeing Company, "About Boeing Commercial Airplanes," , 2020. URL http://www.boeing.com/company/about-bca/.

[49] Nicolai, L. M., and Carichner, G. E., *Fundamentals of Aircraft and Airship Design*, Vol. 1, AIAA, Reston, Virginia, 2010. https://doi.org/10.2514/4.867538.

[50] Jenkinson, L. R., Simpkin, P., and Rhodes, D., *Civil jet aircraft design*, Arnold London, 1999. https://doi.org/10.2514/4.473500.

[51] Airbus S.A.S. Customer Services, "Airbus A320 Aircraft Characteristics Airport and Maintenance Planning," Tech. rep., Airbus S.A.S. Customer Services, 2019.

[52] Boeing Commercial Airplanes, "Boeing 777-200/300 Airplane Characteristics and Airport Planning," Tech. rep., Boeing Commercial Airplanes, 2002.

[53] Swelbar, W. S., and Belobaba, P. P., "Airline Data Project," , 2019. URL http://web.mit.edu/airlinedata/www/default.html.

[54] Husemann, M., Schäfer, K., and Stumpf, E., "Flexibility within flight operations as an evaluation criterion for preliminary aircraft design," *Journal of Air Transport Management*, Vol. 71, 2018, pp. 201–214. https://doi.org/10.1016/j.jairtraman.2018.04.007.

[55] Köhler, M. O., Rädel, G., Dessens, O., Shine, K. P., Rogers, H. L., Wild, O., and Pyle, J. A., "Impact of perturbations to nitrogen oxide emissions from global aviation," *Journal of Geophysical Research: Atmospheres*, Vol. 113, No. D11, 2008. https://doi.org/10.1029/2007JD009140.

[56] Jeßberger, P., Voigt, C., Schumann, U., Sölch, I., Schlager, H., Kaufmann, S., Petzold, A., Schäuble, D., and Gayet, J.-F., "Aircraft type influence on contrail properties," *Atmospheric Chemistry and Physics*, Vol. 13, No. 23, 2013, pp. 11965–11984. https://doi.org/10.5194/acp-13-11965-2013.

[57] IHS Markit, "General Electric GE90," *Jane's Aero-Engines*, IHS Markit, 2019.

[58] York, M. A., Hoburg, W. W., and Drela, M., "Turbofan Engine Sizing and Tradeoff Analysis via Signomial Programming," *Journal of Aircraft*, Vol. 55, No. 3, 2018, pp. 988–1003. https://doi.org/10.2514/1.C034463.

[59] Boeing Commercial Airplanes, "Boeing 737 Airplane Characteristics and Airport Planning," Tech. rep., Boeing Commercial Airplanes, 2013.

[60] Airbus S.A.S. Customer Services, "Airbus A350 Aircraft Characteristics Airport and Maintenance Planning," Tech. rep., Airbus S.A.S. Customer Services, 2020.

[61] Raymer, D., *Aircraft design: a conceptual approach*, American Institute of Aeronautics and Astronautics, Inc., 2012.

[62] Torenbeek, E., *Advanced aircraft design: conceptual design, technology and optimization of subsonic civil airplanes*, John Wiley & Sons, Ltd, Chichester, 2013. https://doi.org/https://doi.org/10.1002/9781118568101.

[63] Torenbeek, E., and Berenschot, G., "De berekening van het omspoeld gonderoppervlak van enkel- en dubbelstroom straalmotoren voor civiele vliegtuigen," Tech. Rep. M-445, Delft University of Technology, Faculty of Aerospace Engineering, 1983.